

RESEARCH ARTICLE

Suppression of epithelial folding at actomyosin-enriched compartment boundaries downstream of Wingless signalling in *Drosophila*

Jose M. Urbano^{1,*}, Huw W. Naylor^{1,*}, Elena Scarpa¹, Leila Muresan^{1,2} and Bénédicte Sanson^{1,‡}

ABSTRACT

Epithelial folding shapes embryos and tissues during development. Here, we investigate the coupling between epithelial folding and actomyosin-enriched compartmental boundaries. The mechanistic relationship between the two is unclear, because actomyosin-enriched boundaries are not necessarily associated with folds. Also, some cases of epithelial folding occur independently of actomyosin contractility. We investigated the shallow folds called parasegment grooves that form at boundaries between anterior and posterior compartments in the early *Drosophila* embryo. We demonstrate that formation of these folds requires the presence of an actomyosin enrichment along the boundary cell-cell contacts. These enrichments, which require Wingless signalling, increase interfacial tension not only at the level of the adherens junctions but also along the lateral surfaces. We find that epithelial folding is normally under inhibitory control because different genetic manipulations, including depletion of the Myosin II phosphatase Flapwing, increase the depth of folds at boundaries. Fold depth correlates with the levels of Bazooka (Baz), the Par-3 homologue, along the boundary cell-cell contacts. Moreover, Wingless and Hedgehog signalling have opposite effects on fold depth at the boundary that correlate with changes in Baz planar polarity.

KEY WORDS: Apico-basal polarity, Contractility, Embryo, Epithelium, Morphogenesis, Planar polarity

INTRODUCTION

Epithelial sheet bending is essential to elaborate the anatomy of animal bodies. It is ubiquitous throughout development, from gastrulation to organogenesis (Bazin-Lopez et al., 2015; Keller and Shook, 2011). The mechanisms identified so far that promote epithelial sheet bending are diverse (Pearl et al., 2017). One of the best-studied mechanisms is apical constriction mediated by actomyosin activation at the apical end of epithelial cells (Martin and Goldstein, 2014). However, not all mechanisms uncovered for

epithelial folding require actomyosin activity; a basal shift of the adherens junctions (AJs) is required instead for dorsal fold formation in *Drosophila* gastrulae (Wang et al., 2012).

Here, we investigate the relationship between epithelial folding and planar actomyosin cables that are often found in developing epithelia (Fagotto, 2015; Monier et al., 2011; Röper, 2013). For example, actomyosin enrichments are found at the level of AJs at compartmental boundaries in *Drosophila* epithelial tissues, forming supracellular contractile cables that are required for lineage restriction (Landsberg et al., 2009; Monier et al., 2010). In some instances, such as in segments, actomyosin-rich cables are associated with folds (Calzolari et al., 2014; Mulinari et al., 2008). In other cases, such as for the anteroposterior (AP) compartmental boundary in *Drosophila* wing discs, actomyosin-rich boundaries are anatomically ‘silent’, with no folding observed (Landsberg et al., 2009). Intriguingly, however, some mutant backgrounds can generate a fold along the AP boundary in wing discs, suggesting that fold formation is normally suppressed at this compartmental boundary (Liu et al., 2016; Shen et al., 2008).

In *Drosophila* embryos, the AP compartmental boundaries (called parasegmental boundaries, PSBs) first enrich actomyosin at gastrulation, during germ-band extension (Tetley et al., 2016). Once the germ-band is extended, Wingless signalling on one side of the compartmental boundary maintains these enrichments, which act as mechanical barriers to keep dividing cells in their compartment of origin (Monier et al., 2010). No epithelial folding is associated with actomyosin-enriched PSBs during gastrulation, and it is only 2 h later, during germ-band extended stages, that shallow indentations form, the parasegmental folds or grooves (Larsen et al., 2008; Martinez-Arias, 1993; Martinez-Arias and Lawrence, 1985). Here, we first establish that actomyosin contractility is required for parasegment fold formation. Next, we provide evidence that fold formation is normally suppressed at PSBs, under the control of Wingless signalling. This moderation of fold formation at PSBs requires Myosin II phosphatase activity and also correlates with the depletion of Bazooka, the homologue of vertebrate Par-3. This shows that specific cellular mechanisms suppress fold formation at actomyosin-rich boundaries.

RESULTS

Wingless signalling maintains earlier planar polarities specifically at the PSBs at germ-band extended stages

The transient parasegmental grooves that form from mid-stage 10 and throughout stage 11 at the site of the compartmental boundaries between Wingless- and Engrailed-expressing cells (PSBs) are absent in *wingless* mutants (Larsen et al., 2008) (Fig. 1A,B). To understand what could control epithelial folding at PSBs downstream of Wingless signalling, we analysed the cortical enrichment of proteins known to be planar polarized earlier in

¹Department of Physiology, Development and Neuroscience, University of Cambridge, Anatomy Building, Downing Street, Cambridge, CB2 3DY, UK.

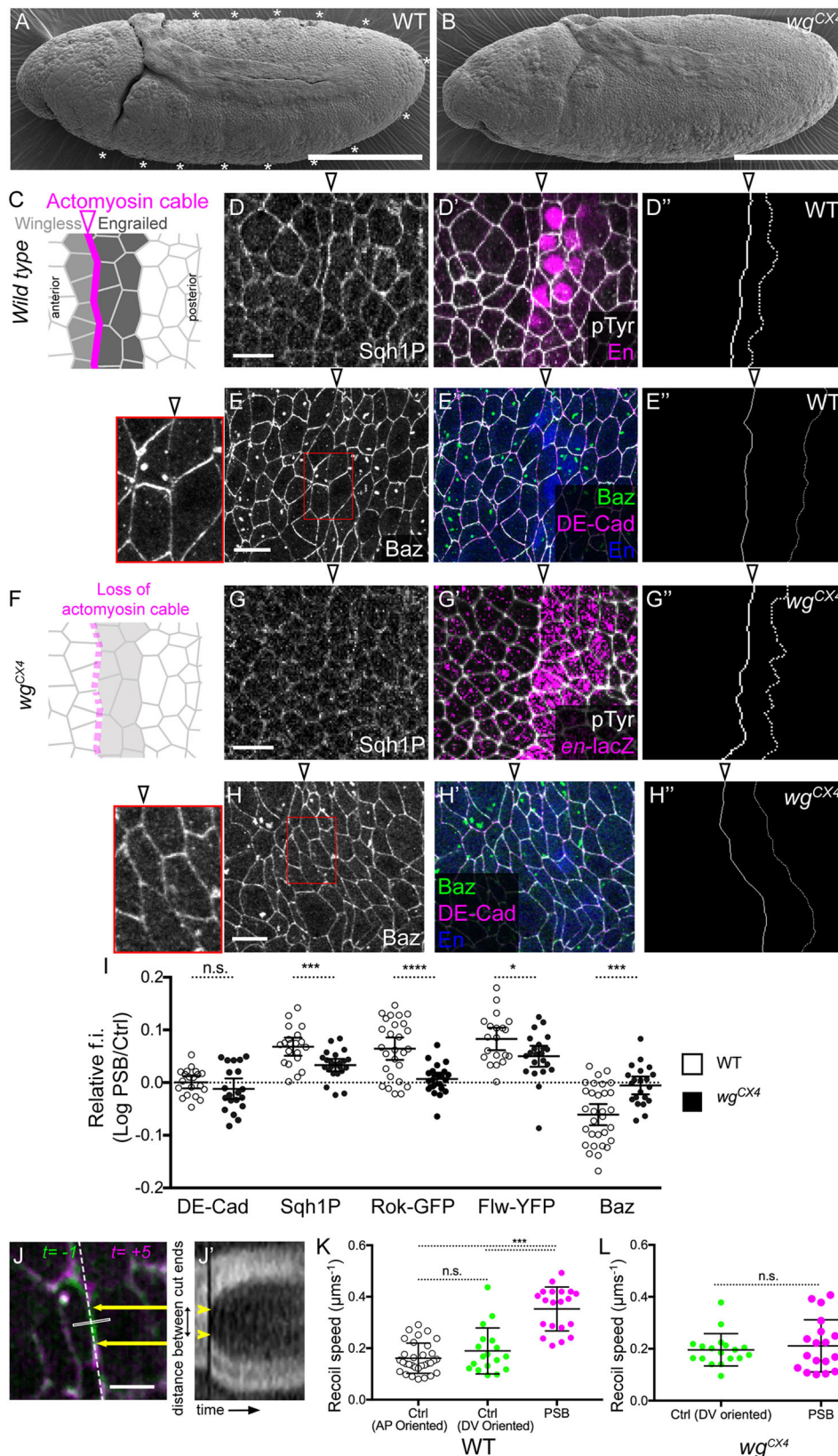
²Cambridge Advanced Imaging Centre, University of Cambridge, Anatomy Building, Downing Street, Cambridge, CB2 3DY, UK.

*These authors contributed equally to this work

‡Author for correspondence (bs251@cam.ac.uk)

© J.M.U., 0000-0002-6644-8129; H.W.N., 0000-0001-8264-8596; E.S., 0000-0002-0849-1276; L.M., 0000-0002-7602-0249; B.S., 0000-0002-2782-4195

This is an Open Access article distributed under the terms of the Creative Commons Attribution License (<http://creativecommons.org/licenses/by/3.0>), which permits unrestricted use, distribution and reproduction in any medium provided that the original work is properly attributed.



development during germ-band extension (stages 7–8) at dorsoventral (DV)-oriented cell-cell junctions, which include early PSBs. For example, F-actin, Myosin II and Rho kinase (Rok) are enriched, whereas Bazooka (Baz, Par-3 homologue) and

E-Cadherin are depleted, at DV-oriented junctions during germ-band extension (Bertet et al., 2004; Blankenship et al., 2006; Farrell et al., 2017; Levayer et al., 2011; Simões et al., 2010; Tetley et al., 2016; Zallen and Wieschaus, 2004). We had shown previously that

F-actin and two reporters for nonmuscle Myosin II, Zip-GFP (*zip* encodes MHC) and Sqh-GFP (*sqh* encodes MRLC), are enriched at PSBs at germ-band extended stages (stages 9 to 11) (Monier et al., 2010). Here, we developed a method to quantify the enrichment or depletion of proteins at the level of AJs along the PSBs, relative to control columns of DV-oriented junctions (see Materials and Methods). We confirm that Myosin II is not only enriched but also activated at the PSBs at germ-band extended stages: the mono-phosphorylated form of MRLC [recognized by the Sqh1P antibody (Zhang and Ward, 2011)] accumulates at the PSB (Fig. 1C-D",I). Moreover, we find that Rok (using Rok-GFP) is enriched at the PSB (Fig. S1B-B"), whereas Baz is depleted (Fig. 1E-E",I). Therefore, the key planar polarities established during germ-band extension are maintained at germ-band-extended stages specifically and robustly at the PSBs.

We find, however, one notable difference in our survey of polarities: whereas E-Cadherin levels are depleted at DV junctions in germ-band extension (Blankenship et al., 2006; Levayer et al., 2011), this does not appear to be the case at PSBs at stage 10, where levels are the same as in other junctions (Fig. 1I, Fig. S1A-A"). This might be linked to the distinct behaviours of cells during axis extension versus boundary formation; when cells intercalate during germ-band extension, contacts need to be remodelled and the depletion of E-Cadherin might facilitate this (Warrington et al., 2013). In contrast, later in development, the PSB is a stable interface between neighbouring cell populations, where normal adhesion might be required for boundary function.

Planar polarities during germ-band extension are under the control of the pair-rule genes (Bertet et al., 2004; Paré et al., 2014; Zallen and Wieschaus, 2004). We have shown recently that PSB interfaces enrich actomyosin more than other DV-oriented interfaces during germ-band extension, and this is also likely to require pair-rule input, because this enrichment is not disrupted in *wingless* mutants (Tetley et al., 2016). In contrast, later on, the maintenance of robust actomyosin polarization at PSBs at germ-band extended stage does require Wingless signalling (Monier et al., 2010). Confirming this, the enrichment of Sqh1P is significantly decreased at PSBs in *wingless* null mutants (Fig. 1F-G",I). Moreover, the enrichment of Rok and depletion of Baz at PSBs is lost (Fig. 1I). Therefore, the maintenance of key planar polarities at the PSBs at germ-band extended stages requires Wingless signalling.

Actomyosin enrichments at PSBs correlate with higher interfacial tension at boundary cell-cell contacts

An actomyosin enrichment along the compartmental boundary interfaces suggests an increase in cortical tension there, which could be important for fold formation. Previously, we had provided evidence of higher tension along the PSBs at germ-band extended stages, by showing that the PSBs are straighter than control DV-oriented columns of interfaces, and that this increased straightness is lost in *wingless* mutants (Monier et al., 2010). Here, we probe more directly junctional tension at the PSBs, using laser ablation to measure the speed of junctional recoil as previously (Tetley et al., 2016). We find that, at stage 10, the recoil velocities are on average about twice as fast at PSBs compared with nonboundary DV- or AP-oriented junctions (Fig. 1J-K). Controls show that the PSB junctions used for ablation are enriched in Myosin II compared with other DV-oriented junctions as expected and their lengths are comparable, ruling out an effect of junction size (Fig. S1D,D').

We repeated the ablations at PSB junctions in a *wingless* mutant, and show that the increase in actomyosin-dependent tension is lost

(Fig. 1L, ablation controls in Fig. S1E,E'). Note that PSBs can be located in *wingless* mutants because of a weak remaining enrichment in actomyosin at the boundary (quantified in Fig. 1I and Fig. S1E) (see also Fig. 2M in Tetley et al., 2016). This weak enrichment is not sufficient to maintain a high tension at the boundary, because both our laser ablation experiments (this study) and quantifications of boundary straightness (Monier et al., 2010) demonstrate that tension at PSB boundaries and control interfaces become identical in *wg^{CX4}* mutants. This confirms that Wingless signalling is required for increasing actomyosin-dependent junctional tension specifically at the PSBs. Because parasegmental groove formation also requires Wingless signalling (Larsen et al., 2008) (Fig. 1B), this result suggests that epithelial folding at PSBs is a consequence of increased junctional actomyosin tension.

Hyperactivation of Myosin II via knockdown of the Myosin II phosphatase Flw increases epithelial folding at PSBs

Although the above results suggest that boundary actomyosin enrichments are required for parasegmental groove formation, they do not appear sufficient. Indeed, we have recently shown that actomyosin enrichments at PSBs are detectable as early as 20 min after the beginning of germ-band extension (stage 8), and that the PSB interfaces are already under higher interfacial tension than other interfaces, as shown by measures of straightness and laser ablation experiments (Tetley et al., 2016). Therefore, the PSBs are continuously enriched in actomyosin from stage 8 onwards (Monier et al., 2010, 2011; Tetley et al., 2016). However, the parasegmental grooves appear only around mid-stage 10, ~2 h later (Martinez-Arias, 1993). This suggests that 'brakes' might exist that limit folding at boundary actomyosin enrichments. A possible 'brake' is Flapwing (Flw), a component of the main phosphatase that negatively regulates nonmuscle Myosin II activity (Vereshchagina et al., 2004). Screening the Cambridge Protein Trap Insertion (CPTI) collection (Lowe et al., 2014; Lye et al., 2014), we have identified Flw-YFP as one of several proteins enriched at PSBs (Naylor, 2011). Here, we show that Flw-YFP is enriched at the PSBs at germ-band extended stages and that this enrichment is significantly reduced in *wingless* null mutants (Fig. 1I, Fig. S1C-C"). We also find that Flw-YFP systematically co-localizes with activated Myosin II (Sqh1P) in early embryos, such as at the cellularization front, the ventral furrow and at DV-oriented cell-cell contacts during germ-band extension (Fig. S2A-C"). Movie 1 also shows that Flw-YFP is dynamically present in medial flows as Myosin II (Rauzi et al., 2010). This suggests an important role of Flw in regulating Myosin II activity at morphogenetic sites.

To disrupt this putative negative regulation, we used the deGradFP system to degrade YFP/GFP-tagged proteins (Caussinus et al., 2012). Because YFP is inserted at the *flw* locus and the resulting Flw-YFP insertion is homozygous viable, all molecules of Flw are susceptible to be degraded. When nanobodies against YFP (*UAS-deGradFP*) are expressed under the control of *paired-Gal4* (*prd-Gal4*), Flw-YFP is efficiently depleted in *prd-Gal4*-expressing domains (Fig. 2A). Although Flw-YFP is normally cortical (Fig. S2A-C"), it is lost from the membranes in the *prd-Gal4* domains and accumulates as bright dots in the cytoplasm (Fig. 2B). We find that Sqh1P levels are elevated in *prd-Gal4* domains (Fig. 2B-B"), indicating that Flw depletion results in Myosin II hyperphosphorylation. We also detect a higher enrichment in Sqh1P along the PSBs located in *prd-Gal4* domains (Fig. 2F). This is consistent with the key reported phenotype of *flw* mutants being an increase in Sqh

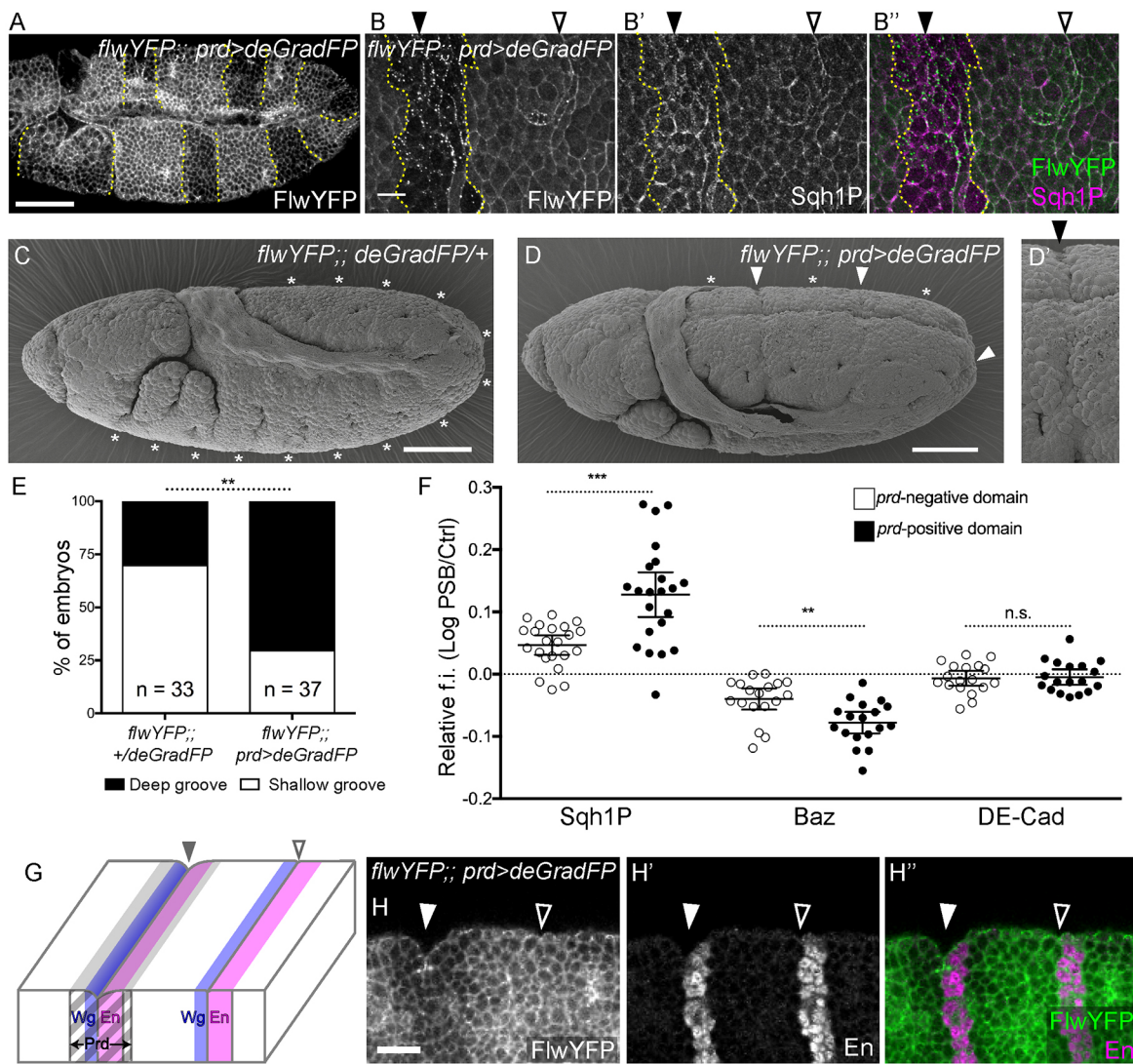


Fig. 2. PSB grooves are deepened by depletion of the Myosin-II phosphatase Flapwing. (A) Immunostaining against GFP reveals degradation of Flw-YFP in an embryo expressing *UAS-deGradFP* in the *prd-Gal4* domain (yellow dotted lines). Scale bar: 50 μ m. (B-B'') The same genotype at higher magnification, immunostained against GFP (B), Sqh1P (B') and merged (B''). Scale bar: 10 μ m. Filled arrowheads indicate PSBs in *prd-Gal4* domains; open arrowheads indicate control PSBs. (C-D') SEM images of late stage 10 control and deGradFP embryos. Asterisks indicate shallow parasegmental grooves in control embryos; filled arrowheads indicate deepened parasegmental grooves in Flw-depleted domains (close-up in D'). Scale bars: 50 μ m. (E) Blind quantification of embryos with shallow only versus deep grooves in sibling embryos shown in C and D. Comparison from Fisher's exact test, $**P=0.0016$. (F) Quantification of the fluorescence intensities (f.i.) of proteins at PSBs in *deGradFP*-expressing and -nonexpressing domains (*prd-Gal4* positive or negative), relative to control interfaces, as \log_{10} (for both domains, Sqh1P, $n=22$ PSBs; Baz and DE-Cad, $n=18$). Error bars show mean \pm 95% CI. Comparisons between *prd-Gal4*-positive and -negative PSBs from Mann-Whitney tests: Sqh1P, $***P=0.0002$; Baz, $**P=0.0016$; DE-Cad, $P=0.9626$ (n.s.). (G) PSB position and fold depth relative to Wg, En and *prd-Gal4* expression domains. (H-H'') Immunostaining against GFP (H) and En (H') (H'', merge) showing the deep groove at the PSB in the Flw-depleted domain (filled arrowheads) and the shallow groove (open arrowheads) in the control domain. Scale bar: 20 μ m.

phosphorylation (Sun et al., 2011; Vereshchagina et al., 2004). To check whether Flw could have other effects, we also quantified some of the planar polarities examined previously. We found that Baz remains depleted at the PSBs in *prd-Gal4* regions (with some increase in the level of depletion) and E-Cadherin is unchanged (Fig. 2F). Because there is a reported effect of Flw on Moesin and Merlin phosphorylation (Yamamoto et al., 2013; Yang et al., 2012), we also quantified phospho-Moesin (pMoe) at the PSBs. We found that pMoe is enriched there, but the level of enrichment did not change in Flw-depleted *prd-Gal4* domains, ruling out this target (Fig. S2D).

Remarkably, deGraFP-mediated Flw depletion is associated with a specific morphogenetic phenotype: the normally shallow

parasegmental grooves (Fig. 2C) are now deep in each *prd-Gal4* domain (Fig. 2D-E, G-H''). This effect is specific to the PSBs: no other epithelial folds appear in the domains depleted for Flw. Together, these results show that Flw negatively regulates fold formation at PSBs, most likely through direct inhibition of Myosin II activity. This indicates that fold formation at PSBs is normally suppressed in wild-type embryos.

Ectopic PSBs are associated with deeper folds compared with endogenous PSBs

To further investigate the link between actomyosin contractility and epithelial folding, we generated ectopic PSBs by expressing *wingless* (*wg*) in the whole epithelium (*arm-Gal4/UAS-wg*,

hereafter *arm>wg*) (Larsen et al., 2008; Sanson et al., 1999). In wild-type embryos, Wg signals at short range from the cells anterior to the PSB, to maintain *engrailed* (*en*) transcription in the cells posterior to the PSB (Vincent and Lawrence, 1994) (Fig. 3A). In *arm>wg* embryos, ectopic Wg maintains *en* expression in a larger domain spanning approximately half the parasegment, which corresponds to the cells competent to transcribe *en* (Fig. 3B). The posterior margin of this enlarged domain now abuts the other half of the parasegment, where cells are competent to transcribe *wg*. This new interface between the enlarged En domain (which also expresses *hedgehog*, *hh*) and the Wg-transcription-competent cells can be viewed as an ectopic PSB, because it replicates the transcriptional and signalling environment of the endogenous PSB. Consistent with this notion, we find that Sqh1P is enriched at the cell-cell contacts of these ectopic PSBs relative to control interfaces, similarly to the endogenous PSBs present in the same embryos (Fig. 3C-E). The positive and negative regulators of Myosin II, Rok and Flw, are also enriched at ectopic PSBs (Fig. 3E). Furthermore, laser ablations of cell-cell contacts at ectopic PSBs show that junctional tension is elevated there as for endogenous PSBs (Fig. 3F, Fig. S3B,B'). We conclude that ectopic PSBs recapitulate the highly contractile actomyosin interfaces of endogenous PSBs.

Ectopic boundaries are associated with an epithelial fold (Larsen et al., 2008), providing additional evidence that actomyosin enrichment at PSBs promotes epithelial folding. There is, however, a key difference: folds at ectopic PSBs are deep when compared with endogenous parasegmental grooves (Fig. 3G-J'). The folding appears even more pronounced than what is observed when actomyosin contractility is elevated in the Flw depletion (compare Fig. 3J' and Fig. 2D'). The deep folds require actomyosin contractility because they are absent (as well as the endogenous grooves) in embryos injected with the Rok inhibitor Y-27632 (Fig. 3K,K'). However, we cannot find evidence of a further increase in junctional actomyosin contractility compared with the endogenous PSBs that could explain the deep folds: enrichments of Sqh1P at ectopic and endogenous PSBs are similar (Fig. 3E) and the recoil speeds upon laser ablation are indistinguishable (Fig. 3F).

To test whether ectopic PSBs were systematically associated with deeper folds, we examined two other genotypes, embryos expressing *rho-Gal4/UAS-wg* (*rho>wg*) and null mutants for the gene *naked cuticle* (*nkd*). *Rho-Gal4* is expressed in a ventral stripe a few cell diameters wide on either side of the ventral midline (Ip et al., 1992). When *wingless* is ectopically expressed using this driver, the En domain is enlarged in the corresponding ventral region and a ventral, stubby, ectopic PSB forms in each parasegment, which is enriched in actomyosin (Fig. S3C,E-E"). A deep fold forms that does not extend beyond the extremity of the short ectopic PSBs, suggesting that the folding might be cell autonomous (Fig. S3D,D'). In a *nkd* null embryo, Wingless signalling is altered and signals more weakly, but over a longer distance, resulting in an enlarged En domain and an ectopic PSB (Martinez Arias et al., 1988; Zeng et al., 2000). These ectopic PSBs enrich actomyosin and produce a deep fold (Fig. S3F-H"). Thus, ectopic PSBs produced by different genetic manipulations all enrich actomyosin at their interfaces like the endogenous PSBs. However, unlike endogenous PSBs, they are systematically associated with deep folds rather than shallow ones.

What could explain the difference in degree of folding between endogenous and ectopic PSBs? We have proposed above that 'brakes' exist that suppress folding at actomyosin-enriched boundaries and shown that Flw is one of these brakes (Fig. 2).

Perhaps not all of the brakes are recapitulated at ectopic boundaries, so we examined the planar polarization of factors we quantified earlier for endogenous boundaries (Fig. 3E). Flw-YFP and Sqh1P are enriched at the same level in both endogenous and ectopic boundaries, which rules out a role for Flapwing. We find, however, clear differences for two other factors: Rok is more enriched at ectopic boundaries, while Baz is no longer depleted (Fig. 3E, Fig. S3A-A"). Because Sqh1P enrichment (also Sqh-GFP enrichment, Fig. S3B) and junctional tension are indistinguishable at endogenous versus ectopic PSBs (Fig. 3E,F), the increase in Rok does not appear to increase junctional actomyosin contractility at the ectopic PSBs. However, it could affect folding through other pathways or modify lateral, rather than junctional contractility (see Discussion). The absence of depletion of Baz at ectopic boundaries was intriguing because Baz has been implicated in the initiation of dorsal folds in the early embryo (Wang et al., 2012). This prompted us to analyse further a putative role of Baz in controlling epithelial fold depth at PSBs.

Bazooka increases the depth of epithelial folding at PSBs

To test whether Baz could have an impact on epithelial folding at PSBs, we overexpressed UAS-Baz-GFP in the embryo using maternal Gal4 drivers (Maternal triple driver, MTD; *MTD>bazGFP*). We find that Baz overexpression causes the formation of deep folds specifically at the PSBs and nowhere else (Fig. 4A-B'). These folds are much deeper than wild-type parasegmental grooves. As for ectopic PSBs in *arm>wg* embryos, this effect cannot be explained by an increase in junctional actomyosin contractility. First, laser ablations of PSB versus control DV-oriented junctions give similar recoil velocities (compare Fig. 4C with Fig. 1K or Fig. 3F), with a ratio of ~2 between PSBs and control junctions (Fig. 4C, controls in Fig. S4B, B'). Second, the absolute quantities of Sqh1P are equivalent between Baz-overexpressing embryos and wild type, for both PSBs and DV-oriented control junctions (Fig. 4F). Third, Sqh1P is similarly enriched at PSBs in both genotypes (Fig. S4A). So in terms of junctional actomyosin enrichment and tension, the PSBs in Baz-overexpressing embryos are indistinguishable from those in wild-type embryos. Note that Baz is still found depleted at PSBs relative to control junctions in Baz-overexpressing embryos (Fig. S4A), suggesting that the signals controlling its depletion at boundaries are functioning normally. As expected, however, the absolute levels of Baz are much higher in Baz-overexpressing embryos (Fig. 4E), indicating that it is the overall increase in Baz that promotes deep epithelial folding at actomyosin-enriched boundaries.

To test this further, we searched for experimental conditions that could rescue deep epithelial folding. We show above that Wingless signalling is required for Baz depletion at the endogenous PSBs (Fig. 1), but that Baz is not depleted at ectopic boundaries in *arm>wg* embryos (Fig. 3). So, a possibility could be that a signal is inhibiting Wingless-dependent depletion of Baz at ectopic boundaries. A likely signal is Hedgehog (Hh) (Hatini and DiNardo, 2001; Sanson, 2001); it has been found to antagonize the regulation of specific genes by Wingless in the region posterior to the Engrailed domain (Sanson et al., 1999) and to increase the lysosomal degradation of Wingless in this region (Dubois et al., 2001). To test whether Hedgehog signalling could have an opposite effect to Wingless signalling on Baz levels, we quantified Baz at ectopic boundaries in *arm>wg* embryos in a null mutant background for *hedgehog* (*arm>wg* [*hh*^{-/-}]). Strikingly in these embryos, fold depth at ectopic boundaries is reduced and now

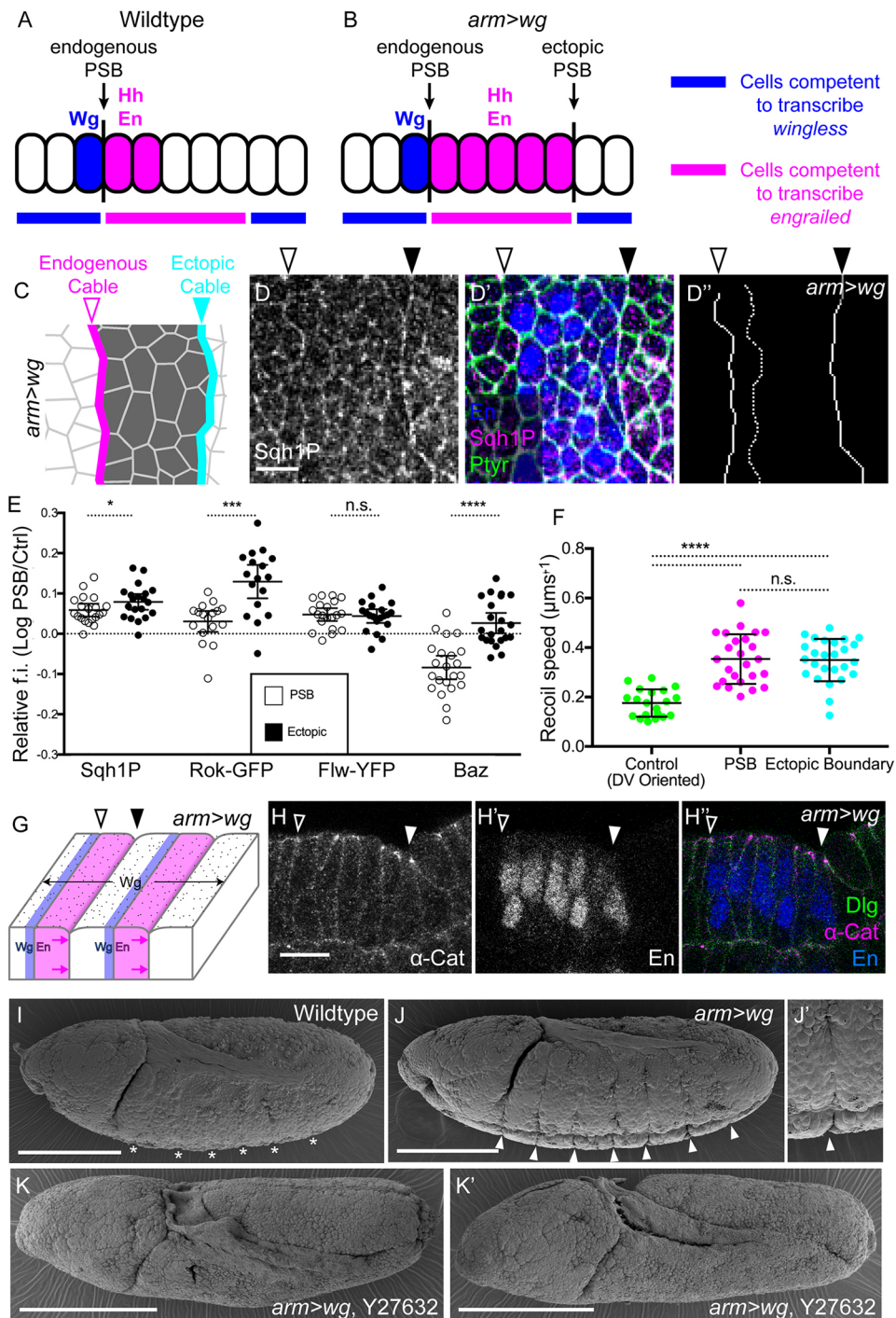


Fig. 3. Increased epithelial folding at ectopic PSBs in *wingless*-overexpressing embryos. (A,B) Location of *wg*-, *hh*- and *en*-expressing cells relative to endogenous and ectopic PSBs at stage 10. Ectopic PSBs form at posterior edges of the enlarged Engrailed domain in *arm>wg* embryos. (C) Position of the actomyosin enrichment at endogenous (magenta) and ectopic (cyan) PSBs in *arm>wg* embryos. (D,D') Immunostaining of *arm>wg* early stage 10 embryos against Sqh1P (D), En and pTyr (merged in D'). Scale bar: 10 μ m. (D'') Traces of endogenous and ectopic PSBs (solid lines) and control junctions (dotted line). (E) Quantification of the fluorescence intensities (f.i.) of proteins in *arm>wg* embryos along the endogenous (open circles) and ectopic (solid circles) PSB junctions, relative to control interfaces, as \log_{10} (for both boundaries, Sqh1P, $n=20$; Rok-GFP, $n=17$; Flw-YFP, $n=20$; Baz, $n=22$). Error bars show mean \pm 95% CI. Comparisons between PSBs and ectopic boundaries from Student's t -tests: Sqh1P, $*P=0.025$; Rok-GFP, $***P=0.0002$; Flw-YFP, $P=0.76$ (n.s.); Baz, $****P<0.0001$. (F) Recoil speeds following laser ablation of endogenous and ectopic PSB cell junctions, and control DV-oriented junctions. Control DV junctions, $n=20$ ablations; PSB, $n=25$; ectopic, $n=26$. Error bars show mean \pm s.d. Comparisons from one-way ANOVA: DV controls versus PSBs or ectopics, $****P<0.0001$; PSB versus ectopics, $P=0.998$ (n.s.). (G) Position of the shallow and deep folds at endogenous and ectopic PSBs, respectively, in *arm>wg* embryos. (H-H'') Sagittal view showing difference in folding at the endogenous and ectopic PSBs of an *arm>wg* embryo stained for alpha-Catenin (α -Cat) (H), En (H') and merged with Discs Large (Dlg) (H''). Scale bar: 10 μ m. (I-J') SEM of stage 10 (I) wild-type and (J,J') *arm>wg* embryos. Endogenous PSBs barely indent the surface of the embryo (asterisks in I), whereas ectopic PSBs form deep grooves (J, close-up in J'). WT, $n=30$ embryos; *arm>wg*, $n=62$ embryos, of which 56 had deep folds. (K,K') SEM of stage 10 *arm>wg* embryos injected with Rho kinase inhibitor Y-27632, showing two examples; $n=10$ embryos, of which 9 had no grooves. Scale bars: 100 μ m. Open arrowheads indicate endogenous PSBs; filled arrowheads indicate ectopic PSBs.

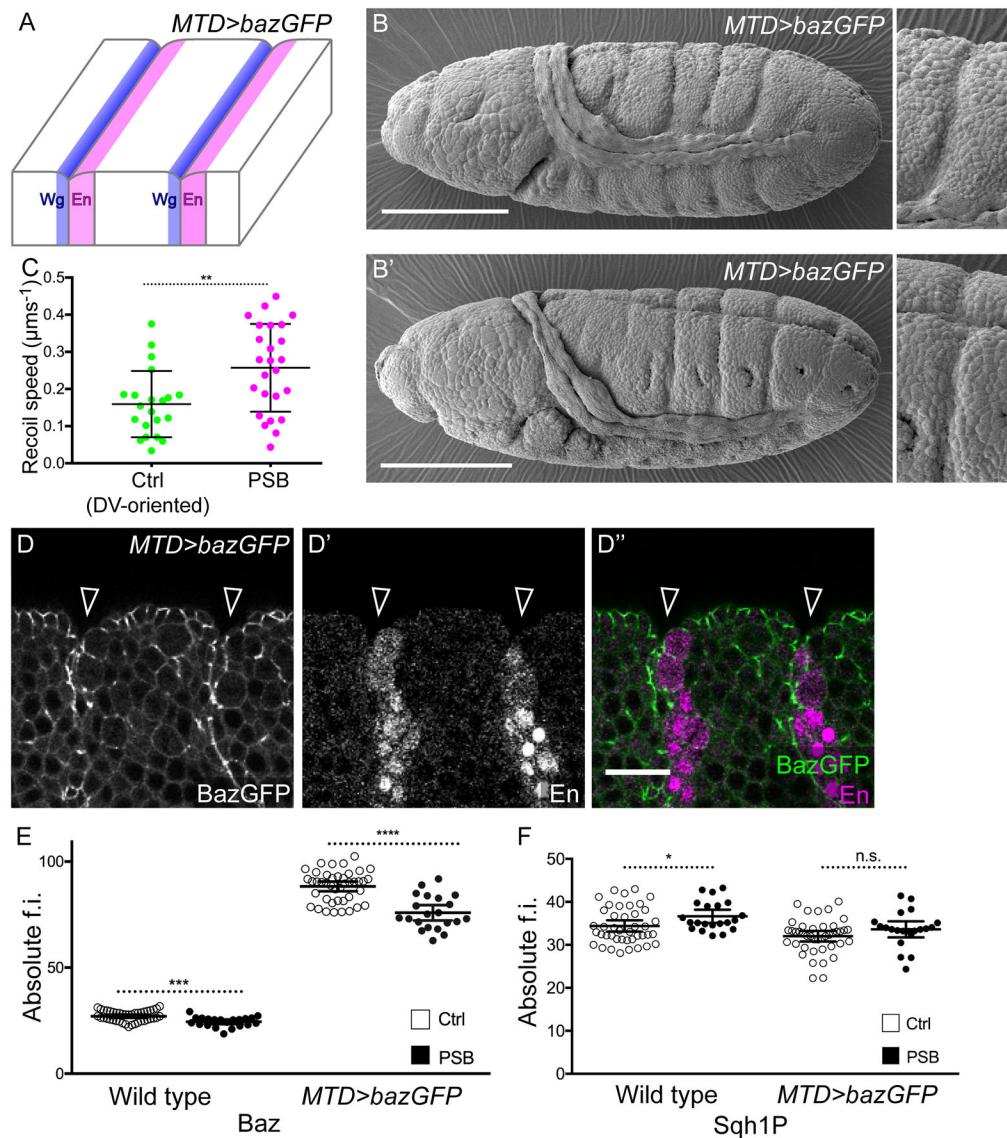


Fig. 4. Baz overexpression increases epithelial folding at actomyosin-enriched boundaries.

(A) Positions of deep folds at endogenous PSBs in *Baz*-overexpressing embryos (*MTD>bazGFP*). (B,B') SEM of *MTD>bazGFP* embryos (B) at stage 10 and (B') stage 11, showing deep folding at PSBs. *n* = 28 embryos (24 show deepened folds, 85.7%). Scale bars: 100 μm. (C) Recoil speeds following laser ablation of DV-oriented control and PSB junctions in *MTD>bazGFP* embryos. Control DV junctions, *n* = 21 ablations; PSB, *n* = 25. Error bars show mean ± s.d. Comparison from a Student's *t*-test: ***P* = 0.0032. (D-D'') Grazing section of an early stage 10 *MTD>bazGFP* embryo, immunostained against GFP (D) and Engrailed (D') (merged in D''), showing deep PSB folds. Scale bar: 20 μm. (E,F) Quantification of the absolute fluorescence intensities (f.i.) of Baz (E) and Sqh1P (F) at PSBs and control DV-oriented interfaces in wild-type and *MTD>bazGFP* embryos, for both Sqh1P and Baz, *n* = 21 boundaries; controls, *n* = 42. Error bars show mean ± 95% CI. Comparisons from Student's *t*-tests: Baz in WT, ****P* = 0.0001; Baz in *MTD>bazGFP*, *****P* < 0.0001; Sqh1P in WT, **P* = 0.0368; Sqh1P in *MTD>bazGFP*, *P* = 0.139 (n.s.).

similar to endogenous boundaries (Fig. 5A-C). Moreover, we find that *Baz* depletion at ectopic boundaries in *arm>wg [hh^{-/-}]* is now indistinguishable from the depletion of *Baz* at endogenous PSBs in *arm>wg* (Fig. 5E) or wild-type (Fig. 1I) embryos. This provides additional evidence that *Wingless* depletes *Baz* levels at endogenous PSBs and, when *Hh* signalling is removed, at ectopic PSBs. Interestingly, the depletion of *Baz* at endogenous boundaries in *arm>wg [hh^{-/-}]* embryos is also enhanced (Fig. 5E), so *Hedgehog* signalling antagonizes *Wingless*-dependent *Baz* depletion at both endogenous and ectopic PSBs. Thus *Wingless* and *Hedgehog* signalling have opposite effects on *Baz* levels at PSBs, endogenous and ectopic. Consistent with findings from *Baz* overexpression embryos (Fig. 4F), we do not find a difference in *Sqh1P* levels in *arm>wg* and *arm>wg [hh^{-/-}]* embryos, for either endogenous or ectopic PSBs (Fig. 5D), indicating that the effect of *Baz* on folding is independent of junctional actomyosin contractility.

The above results are consistent with a role of *Baz* in promoting folding, because its presence at boundaries correlates with folding depth. To test for sufficiency, we attempted to abolish folding by knocking down *Baz*. We used the deGradFP system again, this time

to deplete *Baz*-GFP levels in an *arm>wg* background, to ask whether this would suppress deep folding at ectopic PSBs. We demonstrate first that deGradFP depletion of *Baz*-GFP is effective (Fig. S4C). We then depleted *Baz* levels in embryos which are either homozygous for *Baz*-GFP or transheterozygous for *Baz*-GFP and a null allele of *baz* (*baz^{XR11}*), to test two different levels of depletion. In both cases, the epithelium begins to depolarize (Fig. S4D,E), consistent with the known phenotype of *baz* mutants (Muller and Wieschaus, 1996). However, *Baz* depletion in these embryos is not sufficient to abolish the deep folds at ectopic PSBs. So although *Myosin II* inhibition does suppress folding at both endogenous and ectopic PSBs (Fig. 3K,K'), *Baz* depletion does not. This suggests that either our removal of *Baz* is not early enough in development to inhibit folding or that other factors in addition to *Baz* promote fold formation at PSBs.

Epithelial folding at PSBs is independent of apical constriction or AJ lowering

To understand better the mechanisms leading to folding at PSBs, we examined cell behaviours during both endogenous and ectopic fold formation in live embryos, for a period of 30 min (Fig. 6). We used

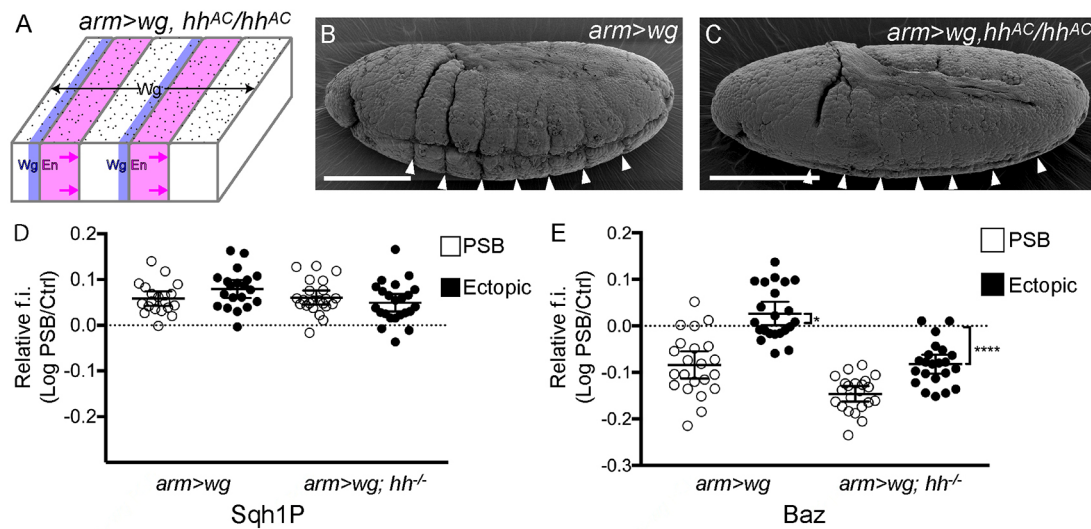


Fig. 5. Fold suppression and Baz depletion is rescued at ectopic PSBs in absence of Hedgehog. (A) Lack of deep grooves at endogenous and ectopic PSBs, in *arm>wg* embryos in a null *hh* mutant background. (B,C) SEM of stage 10 embryos with *arm>wg* (B) showing the deep grooves at ectopic PSBs ($n=62$ embryos), which are much shallower in *arm>wg, hh^{AC}/hh^{AC}* (C) ($n=19$ embryos, of which 17 had shallow grooves). Scale bars: 100 μ m. (D,E) Quantification of the fluorescence intensities (f.i.) of Sqh1P (D) and Baz (E) in *arm>wg* and *arm>wg, hh^{AC}/hh^{AC}* embryos along the PSB (open circles) and ectopic (filled circles) junctions, relative to control cell interfaces, as \log_{10} . Error bars show mean \pm 95% CI. Sqh1P in *arm>wg*, $n=20$; Sqh1P in *arm>wg, hh^{AC}/hh^{AC}*, $n=23$; Baz in *arm>wg*, $n=22$; Baz in *arm>wg, hh^{AC}/hh^{AC}*, $n=22$. Comparisons in E from one-sample Student's *t*-tests: Baz at ectopics in *arm>wg*, difference from 0, $*P=0.0399$; Baz at ectopics in *arm>wg, hh^{AC}/hh^{AC}*, difference from 0, **** $P<0.0001$.

Gap43-Cherry to image the cell membrane and identified PSBs either by the presence of an actomyosin enrichment (reported by Sqh-GFP) for wild-type embryos (Fig. 6A) or by expression of Eve-GFP (which weakly labels cells immediately posterior to the PSBs at this stage) for *arm>wg* embryos (Fig. 6B). During extended germ-band stages (9 to 11), the epidermal cells are dividing frequently (Martinez-Arias, 1993), and in the movie frames shown in Fig. 6, several cells contacting either the endogenous or the ectopic PSBs are dividing. Consistent with our previous finding that the PSB acts as a mechanical barrier (Monier et al., 2010), the resulting daughter cells do not cross the PSBs. However, often the daughter cells move along the PSBs, intercalating between neighbours (Fig. 6, arrowheads). Nondividing boundary cells are also sometimes intercalating (Fig. 6, arrows). Other boundary cells delaminate (Fig. 6, asterisks), having acquired a very elongated apical shape along the boundary. These behaviours suggest that boundary cells are being forced to exchange neighbours, elongate

and sometimes delaminate on either side of the boundary, as a consequence of mechanical tension along the boundary.

These movies, however, did not reveal any obvious, stereotypical cell behaviour that could explain fold formation. Known mechanisms for fold formation include apical constriction (Martin and Goldstein, 2014) and AJ lowering (Wang et al., 2012). In order to use a quantitative approach to search for such mechanisms, we analysed fixed embryos immediately before or just at the beginning of fold formation, imaging the whole cell volume by marking actin using fluorescently labelled phalloidin in WT and *arm>wg* embryos (Fig. 7A-B'). We then segmented the 3D volumes of example cells either abutting PSBs or not (Fig. 7C-F), and measured the position of the AJs relative to the apical top of the cells (see Materials and Methods). In both WT and *arm>wg* embryos, the AJs are a fraction lower ($\sim 0.2 \mu$ m) at PSB interfaces compared with non-PSB interfaces (Fig. 7G,H). However, this lowering is very small compared with the extent of AJ basal shift observed during dorsal

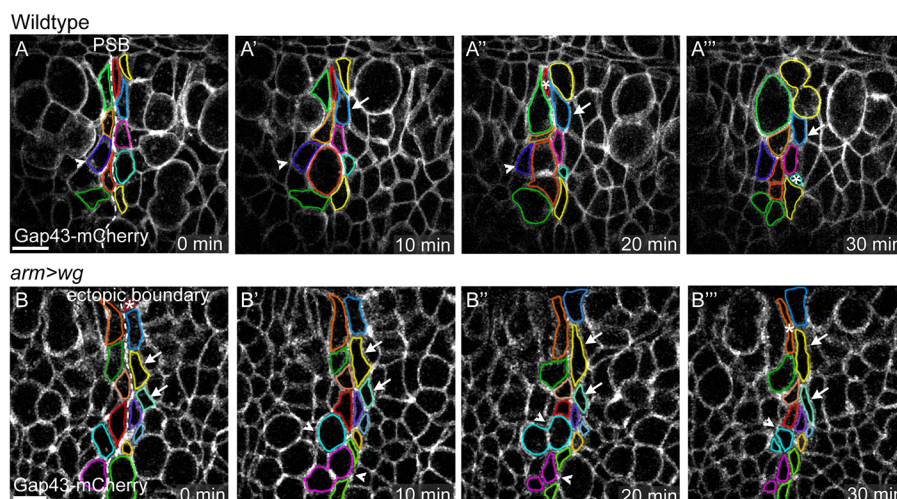


Fig. 6. Cell behaviours during folding at endogenous and ectopic PSBs in live embryos. (A-B'') Frames at 10-min intervals from time-lapse imaging of a live stage 10 embryo expressing Gap43-mCherry, with cells abutting the PSB highlighted, in a wild-type (A-A'') and an *arm>wg* (B-B'') embryo. Dashed lines highlight the boundaries; the asterisks mark cells that delaminate from the epithelium; arrows indicate cells undergoing intercalation; arrowheads indicate cells undergoing intercalation events associated with cell divisions. Anterior is left and ventral is up. Scale bars: 10 μ m.

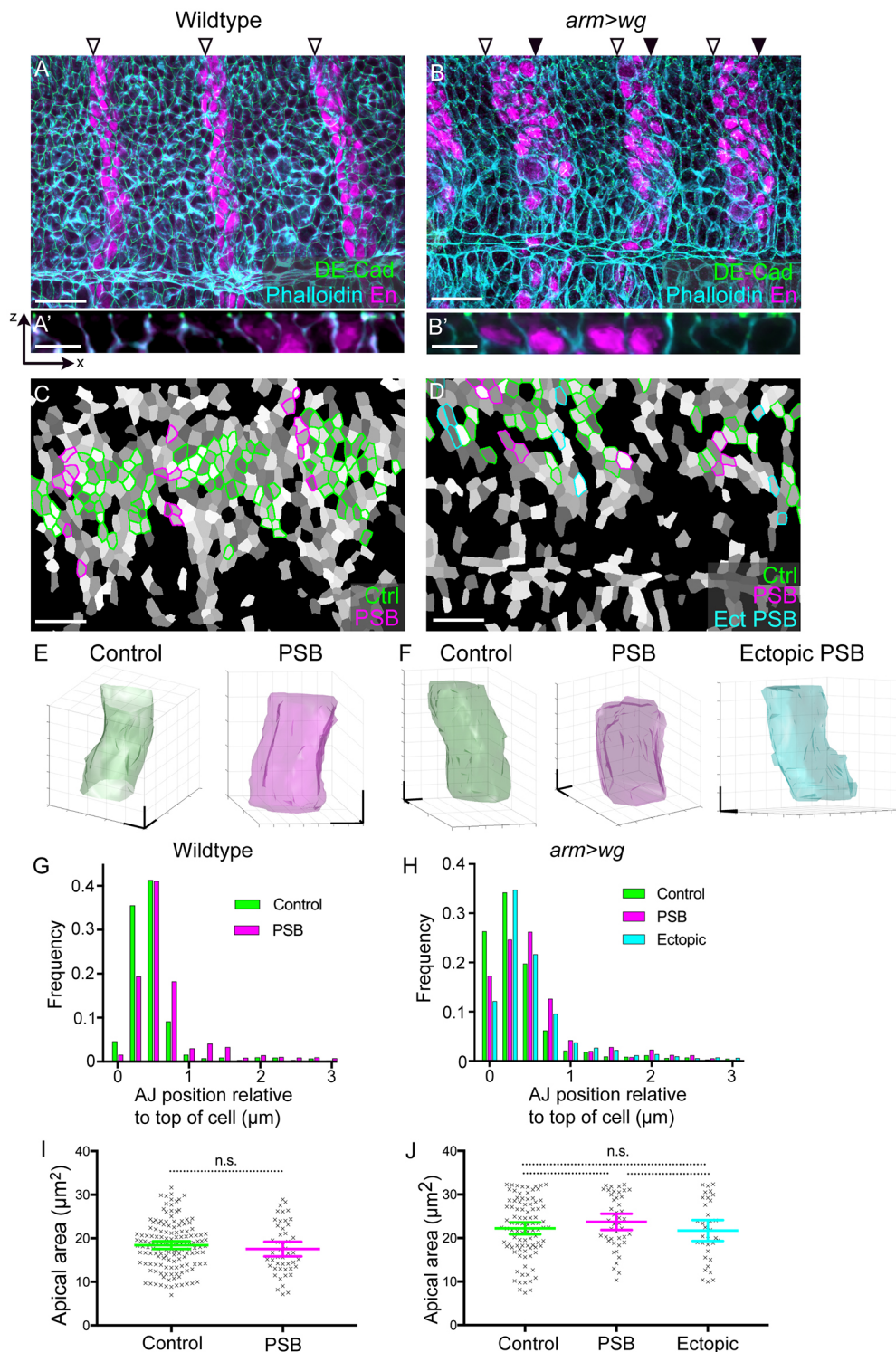


Fig. 7. Measuring AJ lowering and apical constriction at endogenous and ectopic PSBs. (A,B) Confocal stack projections of stage 10 wild-type and *arm>wg* embryos immunostained for E-Cadherin (green), phalloidin (cyan) and Engrailed (magenta). The positions of endogenous (open arrowheads) and ectopic (filled arrowheads) PSBs are indicated. Scale bars: 20 μm . (A',B') Close-up of x-z optical sections through the stacks shown in A and B. Scale bars: 5 μm . (C,D) Cell segmentation of image stacks shown in A and B. Cells depicted in green, magenta and cyan are control cells and endogenous and ectopic PSB-abutting cells, respectively. Scale bars: 20 μm . (E,F) 3D cell reconstructions of representative example cells from wild-type (E) and *arm>wg* (F) embryos. Control cells, green; endogenous PSB-abutting cells, magenta; ectopic PSB-abutting cell, cyan. Scale bars: 2 μm . (G,H) Histograms showing the distance separating the AJs from the top of the cell for control, endogenous PSB and ectopic PSB cell-cell junctions, in wild-type (G) and *arm>wg* (H) embryos. In wild-type embryos, the mean AJ positions are 0.67 μm (below the top of the cell) for controls and 0.86 μm for PSBs ($n=2120$ pixels in PSB junctions; $n=2481$ in controls). In *arm>wg* embryos, the mean AJ positions are 0.71 μm for controls, 0.84 μm for endogenous PSBs and 1.06 μm for ectopic PSBs ($n=1139$ pixels in endogenous PSB junctions; $n=1309$ in controls; $n=1398$ in ectopic PSBs). Outliers ($>3 \mu\text{m}$ between AJ and top of cell) are omitted; they account for 3.1% and 2.5% of the data in wild-type and *arm>wg* embryos, respectively. (I,J) Quantification of apical areas of control cells and cells abutting the endogenous and ectopic PSBs, in wild-type (I) and *arm>wg* (J) embryos (cell numbers: in wild-type controls, $n=144$; PSBs, $n=48$; in *arm>wg* controls, $n=94$; PSBs, $n=44$ PSBs; ectopic PSBs, $n=34$). Comparison in I from a Student's *t*-test: $P=0.338$ (n.s.). Comparisons in J from a Kruskal–Wallis test: all pairs, n.s. Error bars show mean \pm 95% CI. Three embryos of each genotype (shown in Fig. S5) were analysed in G–J.

folding in early embryos, where the junctions of dorsal fold cells lower by up to 10 μm , while neighbouring cells shift their AJs by 3 μm (Wang et al., 2012). We conclude that although both involve Baz, epithelial folding at PSBs is likely to occur via a different mechanism than dorsal folding in gastrulating embryos. We then examined apical cell areas at the level of AJs in WT and *arm>wg* embryos; these are, on average, remarkably similar between nonboundary cells and cells adjacent to either endogenous or ectopic boundaries (Fig. 7I,J). Moreover, sampling the sectional

areas throughout the 3D volume, we could not find any significant differences (Fig. 7E,F and data not shown), suggesting that, on average, there are no significant changes in cell areas between nonboundary and boundary cells, and that apical cell areas are similar to more basal sectional cell areas. We conclude that the boundary cells at endogenous or ectopic PSBs do not undergo apical constriction. Together, these experiments suggest that both AJ lowering (Wang et al., 2012) and apical constriction (Martin and Goldstein, 2014) do not contribute to PSB fold formation.

Several other mechanisms can be considered. One of them is that the increase in actomyosin tension that we detect at the level of the AJs propagates to the lateral domain, below the AJs. An increase in actomyosin contractility in the lateral interfaces could conceivably shorten those and promote folding. Supporting this notion, an increase in actomyosin contractility at the lateral cortex of ascidian endoderm cells is important for their invagination (Sherrard et al., 2010). We reasoned that if this hypothesis is correct, the lateral surfaces should be straighter at PSBs compared with control lateral interfaces. To test this, we segmented the lateral cell surfaces at endogenous and ectopic boundaries as well as control DV interfaces, in wild-type and *arm>wg* embryos (Fig. S5). We then identified the position of the AJs by the peak of intensities in the corresponding channel, and measured an index of straightness for the *z*-planes above and below the AJs. As expected from previous work, the lateral surfaces are straightest at the level of the AJs and become less straight while moving down basally (Fig. S5A,B) (Monier et al., 2010). But, in addition, lateral surfaces at both endogenous and ectopic boundaries are systematically straighter than control lateral surfaces (Fig. S5A-F"). This suggests that the increased tension identified at the level of AJs does propagate basally in boundary cells. This points towards a role of increased lateral membrane contractility in parasegmental groove formation.

DISCUSSION

Actomyosin enrichment at PSBs is required for epithelial folding

In this paper, we demonstrate that the formation of parasegmental grooves requires an actomyosin enrichment at PSBs. Both enrichment and folding occurs at the cell-cell interfaces between *wingless*-expressing cells and *engrailed*-expressing cells, which is the boundary between anterior and posterior compartments in the embryo. In *wingless* mutants, actomyosin enrichments and PSB grooves are both absent (Larsen et al., 2008; Monier et al., 2010; Tetley et al., 2016). When *wingless* is expressed ectopically, either via overexpression using the Gal4 system or in *nkd* mutants, we find an ectopic actomyosin enrichment associated with an ectopic fold in the middle of each parasegment (Fig. 3, Fig. S3). These correlations suggest that parasegmental fold formation requires actomyosin enrichment at the boundaries. Confirming this, inhibition of Myosin II activity using the Rho kinase inhibitor Y-27632 abolishes parasegmental folds, both endogenous and ectopic (Fig. 3K,K'). Thus, inhibition of Myosin II activity is sufficient to disrupt both folding (this study) and boundary straightness (Monier et al., 2010), indicating that these processes are tightly linked. Boundary straightness suggests higher tension along boundary cell-cell contacts, a hallmark of many compartmental and tissue boundaries (Aliee et al., 2012; Amack and Manning, 2012; Calzolari et al., 2014; Fagotto, 2015; Landsberg et al., 2009; Monier et al., 2010; Tetley et al., 2016). Our laser ablations of cell-cell contacts provide direct evidence for this for both endogenous and ectopic PSBs at germ-band extended stages (Fig. 1K, Fig. 3F) and demonstrate that *Wingless* signalling is required for this increase in tension (Fig. 1L).

Our findings about the regulation of actomyosin enrichments are consistent with what is known about the regulation of parasegmental grooves. Larsen et al. (2008) showed that of the segment polarity genes *wingless*, *engrailed* and *hedgehog*, only *wingless* is required for groove formation, which is what we also find for actomyosin enrichments (Monier et al., 2010; Tetley, 2014; Tetley et al., 2016). Actomyosin enrichments at both ectopic and endogenous PSBs are maintained in embryos expressing *wingless* everywhere, in either a

Dfen^E (a small deficiency that removes *engrailed* and its paralogue *invected*) or a *hh^{4C}* background (Tetley, 2014) (Fig. 5D).

We also agree with Larsen et al. (2008) that the role of *Wingless* signalling is permissive rather than instructive. We first detect actomyosin enrichments at PSBs when pair-rule genes are active, during germ-band extension (Tetley et al., 2016). Surprisingly, *Wingless* is not necessary for actomyosin enrichment at PSBs at these early stages (stages 7-8), but is required later, at germ-band extended stages (9-11) (Monier et al., 2010; Tetley et al., 2016). Moreover, when *wingless* is expressed everywhere, only one ectopic actomyosin enrichment is formed, in the middle of each parasegment. This position corresponds to the boundary between the cells competent to transcribe *engrailed* and those competent to transcribe *wingless* (pink and blue domains in Fig. 3B). These two domains are the result of earlier pair-rule gene activities, in particular the activity of the Sloppy paired transcriptional factors (Cadigan et al., 1994; Clark, 2017; Clark and Akam, 2016; Larsen et al., 2008). We conclude that actomyosin enrichments at PSBs are a consequence of earlier pair-rule transcriptional activities, which are maintained by *Wingless* signalling at both endogenous and ectopic boundaries.

Epithelial folding at PSBs is mostly suppressed

Consistent with the above conclusion, we find that some of the planar polarities controlled by pair-rule gene activity during germ-band extension, such as Rok enrichment (Simões et al., 2010) and Baz depletion (Blankenship et al., 2006) are maintained at PSBs at germ-band extended stages, downstream of *Wingless* signalling. In addition, we find that Flapwing, a component of the Myosin II phosphatase (Vereshchagina et al., 2004), is enriched both at PSB cell-cell interfaces (Fig. 1I) and at junctional and medial actomyosin pools during germ-band extension (Movie 1, Fig. S2). Consistent with the latter localization, a role for Myosin II phosphatase in germ-band extension has recently been demonstrated (Munjal et al., 2015). Later, in germ-band extended embryos, the depletion of Flw increases Myosin II activation at PSB cell-cell interfaces and this correlates with the formation of a deeper fold (Fig. 2). This suggests that although actomyosin enrichment is required for fold formation at PSBs, the folding is mostly suppressed. This fits with the observation that parasegmental folds form almost 2 h after actomyosin enrichments are first detected in early embryos and that even at their most prominent (stage 11), they remain modest indentations of the tissue. The known function of actomyosin enrichments at compartmental boundaries is to provide a mechanical barrier to cell mixing (Aliee et al., 2012; Amack and Manning, 2012; Calzolari et al., 2014; Fagotto, 2015; Landsberg et al., 2009; Monier et al., 2010). In *Drosophila* embryos, cell sorting at AP compartmental boundaries is observed before parasegmental groove formation (Monier et al., 2010; Tetley et al., 2016; Vincent and O'Farrell, 1992). In *Drosophila* wing discs, there is no fold associated with the AP boundary, but in some mutant backgrounds a deep fold can form (Liu et al., 2016; Shen et al., 2008). This suggests that fold formation is not required for compartmental cell segregation and also, that for both embryo and disc AP boundaries, the mechanisms of actomyosin enrichment include pathways suppressing epithelial folding.

In addition to the activity of the phosphatase Flw, fold suppression in the embryo might involve the depletion of Baz at actomyosin enriched cell-cell interfaces. Ectopic boundaries have much deeper folds than endogenous boundaries (Larsen et al., 2008; this study), correlating with a loss of Baz depletion (Fig. 3E). Conversely, when Baz is overexpressed, deep folds form at

endogenous PSBs (Fig. 4). Although depletion of Baz requires Wingless signalling, this is counteracted by another signal, Hedgehog (Hh), both at endogenous and ectopic boundaries (Fig. 5E). This suggests that two independent systems, downstream of two distinct signals, have opposite effects on epithelial folding at actomyosin-enriched boundaries. Perhaps Hh signalling is counteracting Wg more effectively later in development, which is why parasegmental folds are most obvious at stage 11 (Martinez-Arias, 1993). Relevant to this, Hh is required from stage 12 onwards for the deep folding at segmental boundaries, located at the posterior edge of the *Engrailed*-expressing cells (Larsen et al., 2003; Mulinari and Hacker, 2009). This deep folding is inhibited by Wingless signalling at the anterior edge of the *engrailed*-expressing cells, so the antagonistic interaction between Wg and Hh is also relevant to segmental fold formation. At segmental boundaries, Hh signalling is thought to cause apical constriction (Larsen et al., 2003; Mulinari and Hacker, 2009) and this requires Myosin II activation (Mulinari et al., 2008). Interestingly, a role for Hh signalling in Myosin II-dependent apical constriction has also been shown for morphogenetic furrow formation in *Drosophila* eye discs (Corrigall et al., 2007; Escudero et al., 2007). So Wingless signalling might be inhibiting Hh-dependent apical constriction at both parasegmental and segmental boundaries, perhaps by promoting the planar polarization of factors such as Baz.

Our Baz depletion experiments did not abolish the deep folding at ectopic boundaries (Fig. S4C-E), suggesting that Baz is only one of the components in a fold-suppression pathway. An obvious candidate might be Rok as it is known to remove Baz from actomyosin-enriched junctions during germ-band extension (Simões et al., 2010). At PSBs, Rok is enriched and this enrichment requires Wingless signalling like the other polarities (Fig. 1I). At ectopic boundaries, this enrichment increases further (Fig. 3E), so there is no simple relationship between Rok localization and Baz depletion at the PSBs. However, the fact that both factors change at ectopic boundaries might indicate that they are both important in fold regulation and might be co-regulated. Because localization of Rok, however, is not necessarily indicative of its activity, monitoring upstream Rho activity is likely to be more informative (Munjal et al., 2015).

Epithelial folding at PSBs occurs through a novel mechanism

We propose that two pathways compete at PSBs: Wingless signalling maintains robust actomyosin enrichment at the boundary while preventing folding, whereas Hedgehog signalling promotes folding. The balance between the two would produce shallow folds at endogenous PSBs and deeper folds at ectopic PSBs. To understand the underlying cell biology, we have examined boundary cell behaviours in live and fixed embryos. From analysis of fixed embryos, we cannot detect any significant apical constriction or lowering of AJs in boundary cells (Fig. 7). One caveat of this analysis is that we use embryos at the beginning of fold formation, because of the difficulties of doing image segmentation on already folded embryos. However, our movies of live embryos during folding did not reveal any obvious stereotypical behaviours (Fig. 6). Instead, we observed a range of behaviours (delaminations, cell intercalations, cell elongation along the boundary) suggesting that cells are being displaced and deformed as a consequence of the increased tension at the boundary. We show that boundary tension is not only evident at the level of AJs, but also propagates to the lateral surface (Fig. S5). The simplest hypothesis is that straightening of the PSB lateral surface as a consequence of increased contractility leads

to its shortening in the apico-basal axis, producing an indentation in the tissue, explaining the parasegmental grooves. Supporting this, increased lateral contractility in ascidian gastrulation has been shown to cause endoderm cell shortening (Sherrard et al., 2010). Interestingly, a combination of Myosin II-dependent indentation of the epithelium and cell loss through apoptosis underlies folding during leg joint formation in *Drosophila* (Monier et al., 2015). Computational modelling suggests that tissue curvature is important for fold formation in this example. Based on this, it is conceivable that increased lateral contractility, cell displacements at the boundary (Fig. 6) and embryo curvature might all contribute to fold formation at PSBs.

An increase in junctional and/or lateral contractility, however, does not readily explain the presence of deep folds at ectopic PSBs or at endogenous PSBs when Baz is overexpressed. Indeed, we did not find an increase in actomyosin concentration or interfacial tension at the level of the AJs (for example, Fig. 3E,F) and the lateral surfaces at ectopic boundaries are not straighter than those at endogenous boundaries (Fig. S5B). However, we have not measured directly either actomyosin enrichment or tension along lateral surfaces, so we cannot, at present, rule out a difference in these.

Our correlations suggest that levels of Baz along actomyosin-enriched cell-cell contacts could influence epithelial folding. There is growing evidence that Baz affects E-Cadherin dynamics (Bulgakova et al., 2013; Coopman and Djiane, 2016; Truong Quang et al., 2013; Weng and Wieschaus, 2017). E-Cadherin turnover or distribution could be subtly different at endogenous versus ectopic boundaries because of the difference in Baz levels. This could in turn modify the mechanical coupling between E-Cadherin and actomyosin networks (Heer and Martin, 2017; Lecuit and Yap, 2015; Röper, 2015). So, comparable actomyosin enrichments might lead to different deformations, depending on E-Cadherin distribution/turnover. For example, an isotropic distribution of E-Cadherin around the cell is important for effective constriction of apical cell areas (Coravos and Martin, 2016; Lv and Großhans, 2016). More work is needed to understand how the polarization of Baz could affect E-Cadherin dynamics and in turn modify 3D cell shapes. Baz depletion is often associated with actomyosin cable-like enrichments in the absence of folds (Osterfield et al., 2013; Röper, 2013; St Johnston and Sanson, 2011; Tamada and Zallen, 2015), so the suppression of fold formation at actomyosin-enriched boundaries via specific planar asymmetries (here maintained by Wingless signalling and counteracted by Hedgehog signalling) might be relevant beyond PSBs.

MATERIALS AND METHODS

Fly strains

The mutant alleles and constructs used in this study are listed in the supplementary Materials and Methods. Genotypes are provided in Table S1. Gene information is from FlyBase (Gramates et al., 2017).

Immunostaining

Standard protocols were used to fix embryos and are described in full, along with a list of primary antibodies, in the supplementary Materials and Methods.

PSB enrichment imaging and analysis

Fixed embryos were imaged by standard confocal optical sectioning and enrichment was analysed in stage 10 embryos, except for *arm>wg*, for which late stage 9 embryos were used to avoid too much folding at the ectopic boundaries. Quantification of protein enrichment was performed in

maximum intensity projections of *z* optical slices containing the AJs. Three-pixel-wide traces along PSBs or control DV-oriented cell-cell contacts were drawn using ImageJ plug-ins. Average fluorescence intensities from the traces were background subtracted first, then PSB enrichment or depletion was calculated by dividing the PSB fluorescence intensity for a given marker by the fluorescence intensity for a nearby control DV-oriented trace. The log₁₀ of these ratios were plotted to restore symmetry between enrichments and depletions on the plots and facilitate statistical comparisons.

3D image segmentation, quantification of cell areas, AJ position and index of straightness

Stage 10 wild-type and *arm>wg* embryos were fixed and immunostained for En, E-Cadherin and phalloidin to label the PSBs, AJs and cell contours, respectively. Note that *arm>wg* embryos were a little younger than wild type to minimize folding at ectopic boundaries; earlier staging is evident from the midline cells not yet being invaginated in *arm>wg* embryos (Fig. S5E,E''), in contrast to wild-type embryos (Fig. S5C,C'') (Martinez-Arias, 1993).

Embryos were imaged by standard confocal imaging, optically sectioning from the top to the bottom of the cell. The actin phalloidin signal was used to segment the 3D shapes of the cells. Segmented cells either abutting the endogenous or ectopic boundaries, or away from the boundaries as controls, were selected for quantitative analysis. Cell areas were quantified for each optical slice, including an apical slice corresponding to the AJs presented in Fig. 7I,J.

For measuring AJ positions and indices of straightness, line traces were generated at the level of AJs as for quantifying PSB enrichment/depletion. These traces were propagated to find the cells' apico-basal surfaces above and below AJs (dividing cells were discarded). An estimate of the cell top was calculated and used to measure the distance between top of the cell and AJ position, for each cell. An index of straightness was calculated for each line trace propagated at each *z* position above and below AJs.

Scanning electron microscopy

Embryos were fixed, dehydrated and gold coated following standard protocols, then imaged with the scanning electron microscopy (SEM) from the Cambridge Advanced Imaging Centre (CAIC).

Embryo drug injections

Rok inhibitor Y-27632 at 1 mM was injected into the yolk of early stage 9 *arm>wg* embryos. We established previously that, presumably because of the whole embryo dilution, this concentration is not sufficient to block cell division, but is sufficient to disrupt boundary formation because PSBs lose their characteristic straightness (Monier et al., 2010). Embryos were aged until stage 10, then fixed and manually devitellinized. A secondary fixation was performed to process the embryos for SEM as above.

Live imaging

Embryos were dechorionated in bleach and imaged in halocarbon oil, using either a spinning disc confocal (Fig. 6) or for performing ablations, a two-photon confocal microscope, see below.

Laser ablation

A near-infrared laser delivering femtosecond pulses coupled to a two-photon confocal microscope (in CAIC), was used to perform ablations in embryos carrying *sqh-GFP* in different genotypes (Table S1). Line ablations ~2 µm long were performed in the middle of a cell-cell contact at the level of AJs. Kymographs imaging *sqh-GFP* signal before and after ablation were used to quantify the recoil velocity of cut ends over time.

Further details for each of the above sections are provided in the supplementary Materials and Methods.

Acknowledgements

We thank Jeremy Skepper, Karin Müller and Kevin O'Holleran, from the Cambridge Advanced Imaging Centre (<http://caic.bio.cam.ac.uk/>) for help with SEM and laser ablation experiments, and Rob Tetley for the images in Fig. S3E,E',H,H'. We

acknowledge FlyBase (<http://flybase.org/>) for gene information, and Emmanuel Caussinus, Vincent Mirouse, Robert E. Ward IV, Andreas Wodarz and Bloomington *Drosophila* Stock Center (<https://bdsc.indiana.edu/>) for *Drosophila* strains and reagents. We thank Erik Clark, Claire Lye, Tom Sharrock and Nic Tapon for critical reading of the manuscript, and members of Bénédicte Sanson's research group for discussions.

Competing interests

The authors declare no competing or financial interests.

Author contributions

Conceptualization: B.S.; Methodology: J.M.U., H.W.N., E.S., L.M.; Software: L.M.; Validation: J.M.U., H.W.N., E.S.; Investigation: J.M.U., H.W.N., E.S., B.S.; Data curation: H.W.N.; Writing - original draft: B.S.; Writing - review & editing: J.M.U., H.W.N., E.S., B.S.; Project administration: B.S.; Funding acquisition: B.S.

Funding

This work was supported by the Biotechnology and Biological Sciences Research Council (BBSRC) [BB/J010278/1] and the Wellcome Trust [099234/Z/12/Z to B.S.; 099130/Z/12/Z to CAIC]. J.M.U. was supported by a Postdoctoral Fellowship [I-D+I 2008-2011] from Ministerio de Educación, Cultura y Deporte (Spanish Ministry of Education), E.S. by a University of Cambridge Herchel Smith Postdoctoral Fellowship and L.M. by an Engineering and Physical Sciences Research Council (EPSRC) Research Software Engineer Fellowship. Deposited in PMC for immediate release.

Supplementary information

Supplementary information available online at <http://dev.biologists.org/lookup/doi/10.1242/dev.155325.supplemental>

References

- Aliee, M., Röper, J.-C., Landsberg, K. P., Pentzold, C., Widmann, T. J., Jülicher, F. and Dahmann, C. (2012). Physical mechanisms shaping the *Drosophila* dorsoventral compartment boundary. *Curr. Biol.* **22**, 967-976.
- Amack, J. D. and Manning, M. L. (2012). Knowing the boundaries: extending the differential adhesion hypothesis in embryonic cell sorting. *Science* **338**, 212-215.
- Bazin-Lopez, N., Valdivia, L. E., Wilson, S. W. and Gestri, G. (2015). Watching eyes take shape. *Curr. Opin. Genet. Dev.* **32**, 73-79.
- Bertet, C., Sulak, L. and Lecuit, T. (2004). Myosin-dependent junction remodelling controls planar cell intercalation and axis elongation. *Nature* **429**, 667-671.
- Blankenship, J. T., Backovic, S. T., Sanny, J. S. P., Weitz, O. and Zallen, J. A. (2006). Multicellular rosette formation links planar cell polarity to tissue morphogenesis. *Dev. Cell* **11**, 459-470.
- Bulgakova, N. A., Grigoriev, I., Yap, A. S., Akhmanova, A. and Brown, N. H. (2013). Dynamic microtubules produce an asymmetric E-cadherin-Bazooka complex to maintain segment boundaries. *J. Cell Biol.* **201**, 887-901.
- Cadigan, K. M., Grossniklaus, U. and Gehring, W. J. (1994). Localized expression of sloppy paired protein maintains the polarity of *Drosophila* parasegments. *Genes Dev.* **8**, 899-913.
- Calzolari, S., Terriente, J. and Pujades, C. (2014). Cell segregation in the vertebrate hindbrain relies on actomyosin cables located at the interhombomeric boundaries. *EMBO J.* **33**, 686-701.
- Caussinus, E., Kanca, O. and Affolter, M. (2012). Fluorescent fusion protein knockout mediated by anti-GFP nanobody. *Nat. Struct. Mol. Biol.* **19**, 117-121.
- Clark, E. (2017). Dynamic patterning by the *Drosophila* pair-rule network reconciles long-germ and short-germ segmentation. *PLoS Biol.* **15**, e2002439.
- Clark, E. and Akam, M. (2016). Odd-paired controls frequency doubling in *Drosophila* segmentation by altering the pair-rule gene regulatory network. *eLife* **5**, e18215.
- Coopman, P. and Djiane, A. (2016). Adherens junction and E-Cadherin complex regulation by epithelial polarity. *Cell. Mol. Life Sci.* **73**, 3535-3553.
- Coravos, J. S. and Martin, A. C. (2016). Apical sarcomere-like actomyosin contracts nonmuscle *Drosophila* epithelial cells. *Dev. Cell* **39**, 346-358.
- Corrigall, D., Walther, R. F., Rodriguez, L., Fichelson, P. and Pichaud, F. (2007). Hedgehog signaling is a principal inducer of Myosin-II-driven cell ingression in *Drosophila* epithelia. *Dev. Cell* **13**, 730-742.
- Dubois, L., Lecourtis, M., Alexandre, C., Hirst, E. and Vincent, J.-P. (2001). Regulated endocytic routing modulates wingless signaling in *Drosophila* embryos. *Cell* **105**, 613-624.
- Escudero, L. M., Bischoff, M. and Freeman, M. (2007). Myosin II regulates complex cellular arrangement and epithelial architecture in *Drosophila*. *Dev. Cell* **13**, 717-729.
- Fagotto, F. (2015). Regulation of cell adhesion and cell sorting at embryonic boundaries. *Curr. Top. Dev. Biol.* **112**, 19-64.
- Farrell, D. L., Weitz, O., Magnasco, M. O. and Zallen, J. A. (2017). SEGGA: a toolset for rapid automated analysis of epithelial cell polarity and dynamics. *Development* **144**, 1725-1734.

- Gramates, L. S., Marygold, S. J., Santos, G. D., Urbano, J.-M., Antonazzo, G., Matthews, B. B., Rey, A. J., Tabone, C. J., Crosby, M. A., Emmert, D. B. et al. (2017). FlyBase at 25: looking to the future. *Nucleic Acids Res.* **45**, D663-D671.
- Hatini, V. and DiNardo, S. (2001). Divide and conquer: pattern formation in *Drosophila* embryonic epidermis. *Trends Genet.* **17**, 574-579.
- Heer, N. C. and Martin, A. C. (2017). Tension, contraction and tissue morphogenesis. *Development* **144**, 4249-4260.
- Ip, Y. T., Park, R. E., Kosman, D., Bier, E. and Levine, M. (1992). The dorsal gradient morphogen regulates stripes of rhomboid expression in the presumptive neuroectoderm of the *Drosophila* embryo. *Genes Dev.* **6**, 1728-1739.
- Keller, R. and Shook, D. (2011). The bending of cell sheets—from folding to rolling. *BMC Biol.* **9**, 90.
- Landsberg, K. P., Farhadifar, R., Ranft, J., Umetsu, D., Widmann, T. J., Bittig, T., Said, A., Jülicher, F. and Dahmann, C. (2009). Increased cell bond tension governs cell sorting at the *Drosophila* anteroposterior compartment boundary. *Curr. Biol.* **19**, 1950-1955.
- Larsen, C. W., Hirst, E., Alexandre, C. and Vincent, J.-P. (2003). Segment boundary formation in *Drosophila* embryos. *Development* **130**, 5625-5635.
- Larsen, C., Bardet, P.-L., Vincent, J.-P. and Alexandre, C. (2008). Specification and positioning of parasegment grooves in *Drosophila*. *Dev. Biol.* **321**, 310-318.
- Lecuit, T. and Yap, A. S. (2015). E-cadherin junctions as active mechanical integrators in tissue dynamics. *Nat. Cell Biol.* **17**, 533-539.
- Levayer, R., Pelissier-Monier, A. and Lecuit, T. (2011). Spatial regulation of Dia and Myosin-II by RhoGEF2 controls initiation of E-cadherin endocytosis during epithelial morphogenesis. *Nat. Cell Biol.* **13**, 529-540.
- Liu, S., Sun, J., Wang, D., Pflugfelder, G. O. and Shen, J. (2016). Fold formation at the compartment boundary of *Drosophila* wing requires Yki signaling to suppress JNK dependent apoptosis. *Sci. Rep.* **6**, 38003.
- Lowe, N., Rees, J. S., Roote, J., Ryder, E., Armean, I. M., Johnson, G., Drummond, E., Spriggs, H., Drummond, J., Magbanua, J. P. et al. (2014). Analysis of the expression patterns, subcellular localisations and interaction partners of *Drosophila* proteins using a pigP protein trap library. *Development* **141**, 3994-4005.
- Lv, Z. and Großhans, J. (2016). A radial actin network in apical constriction. *Dev. Cell* **39**, 280-282.
- Lye, C. M., Naylor, H. W. and Sanson, B. (2014). Subcellular localisations of the CPTI collection of YFP-tagged proteins in *Drosophila* embryos. *Development* **141**, 4006-4017.
- Martin, A. C. and Goldstein, B. (2014). Apical constriction: themes and variations on a cellular mechanism driving morphogenesis. *Development* **141**, 1987-1998.
- Martinez-Arias, A. (1993). Development and patterning of the larval epidermis of *Drosophila*. In *The Development of Drosophila melanogaster* (ed. M. Bate and A. Martinez-Arias), pp. 517-608. Cold Spring Harbor, NY: Cold Spring Harbor Laboratory Press.
- Martinez-Arias, A. and Lawrence, P. A. (1985). Parasegments and compartments in the *Drosophila* embryo. *Nature* **313**, 639-642.
- Martinez Arias, A., Baker, N. E. and Ingham, P. W. (1988). Role of segment polarity genes in the definition and maintenance of cell states in the *Drosophila* embryo. *Development* **103**, 157-170.
- Monier, B., Pélissier-Monier, A., Brand, A. H. and Sanson, B. (2010). An actomyosin-based barrier inhibits cell mixing at compartmental boundaries in *Drosophila* embryos. *Nat. Cell Biol.* **12**, 60-65.
- Monier, B., Pélissier-Monier, A. and Sanson, B. (2011). Establishment and maintenance of compartmental boundaries: role of contractile actomyosin barriers. *Cell. Mol. Life Sci.* **68**, 1897-1910.
- Monier, B., Gettings, M., Gay, G., Mangeat, T., Schott, S., Guarner, A. and Suzanne, M. (2015). Apico-basal forces exerted by apoptotic cells drive epithelium folding. *Nature* **518**, 245-248.
- Mulinari, S. and Hacker, U. (2009). Hedgehog, but not Odd skipped, induces segmental grooves in the *Drosophila* epidermis. *Development* **136**, 3875-3880.
- Mulinari, S., Barmchi, M. P. and Hacker, U. (2008). DRhoGEF2 and diaphanous regulate contractile force during segmental groove morphogenesis in the *Drosophila* embryo. *Mol. Biol. Cell* **19**, 1883-1892.
- Muller, H. A. and Wieschaus, E. (1996). armadillo, bazooka, and stardust are critical for early stages in formation of the zonula adherens and maintenance of the polarized blastoderm epithelium in *Drosophila*. *J. Cell Biol.* **134**, 149-163.
- Munjal, A., Philippe, J.-M., Munro, E. and Lecuit, T. (2015). A self-organized biomechanical network drives shape changes during tissue morphogenesis. *Nature* **524**, 351-355.
- Naylor, H. W. (2011). A combined screening and candidate approach to finding novel Myosin II regulators in *Drosophila* morphogenesis. MPhil thesis, Department of Physiology, Development and Neuroscience, University of Cambridge.
- Osterfield, M., Du, X. X., Schüpbach, T., Wieschaus, E. and Shvartsman, S. Y. (2013). Three-dimensional epithelial morphogenesis in the developing *Drosophila* egg. *Dev. Cell* **24**, 400-410.
- Paré, A. C., Vichas, A., Fincher, C. T., Mirman, Z., Farrell, D. L., Mainieri, A. and Zallen, J. A. (2014). A positional Toll receptor code directs convergent extension in *Drosophila*. *Nature* **515**, 523-527.
- Pearl, E. J., Li, J. and Green, J. B. A. (2017). Cellular systems for epithelial invagination. *Philos. Trans. R. Soc. Lond. B Biol. Sci.* **372**, 20150526.
- Rauzi, M., Lenne, P.-F. and Lecuit, T. (2010). Planar polarized actomyosin contractile flows control epithelial junction remodelling. *Nature* **468**, 1110-1114.
- Röper, K. (2013). Supracellular actomyosin assemblies during development. *Bioarchitecture* **3**, 45-49.
- Röper, K. (2015). Integration of cell-cell adhesion and contractile actomyosin activity during morphogenesis. *Curr. Top. Dev. Biol.* **112**, 103-127.
- Sanson, B. (2001). Generating patterns from fields of cells. Examples from *Drosophila* segmentation. *EMBO Rep.* **2**, 1083-1088.
- Sanson, B., Alexandre, C., Fascetti, N. and Vincent, J.-P. (1999). Engrailed and hedgehog make the range of Wingless asymmetric in *Drosophila* embryos. *Cell* **98**, 207-216.
- Shen, J., Dörner, C., Bahlo, A. and Pflugfelder, G. O. (2008). optomotor-blind suppresses instability at the A/P compartment boundary of the *Drosophila* wing. *Mech. Dev.* **125**, 233-246.
- Sherrard, K., Robin, F., Lemaire, P. and Munro, E. (2010). Sequential activation of apical and basolateral contractility drives ascidian endoderm invagination. *Curr. Biol.* **20**, 1499-1510.
- Simões, S. D. M., Blankenship, J. T., Weitz, O., Farrell, D. L., Tamada, M., Fernandez-Gonzalez, R. and Zallen, J. A. (2010). Rho-kinase directs Bazooka/Par-3 planar polarity during *Drosophila* axis elongation. *Dev. Cell* **19**, 377-388.
- St Johnston, D. and Sanson, B. (2011). Epithelial polarity and morphogenesis. *Curr. Opin. Cell Biol.* **23**, 540-546.
- Sun, Y., Yan, Y., Deneff, N. and Schupbach, T. (2011). Regulation of somatic myosin activity by protein phosphatase 1 β controls *Drosophila* oocyte polarization. *Development* **138**, 1991-2001.
- Tamada, M. and Zallen, J. A. (2015). Square cell packing in the *Drosophila* embryo through spatiotemporally regulated EGF receptor signaling. *Dev. Cell* **35**, 151-161.
- Tetley, R. J. (2014). Linking actomyosin patterning with cell behaviours at compartment boundaries in *Drosophila* embryos. PhD thesis, Department of Physiology, Development and Neuroscience, University of Cambridge.
- Tetley, R. J., Blanchard, G. B., Fletcher, A. G., Adams, R. J. and Sanson, B. (2016). Unipolar distributions of junctional Myosin II identify cell stripe boundaries that drive cell intercalation throughout *Drosophila* axis extension. *eLife* **5**, e12094.
- Truong Quang, B.-A., Mani, M., Markova, O., Lecuit, T. and Lenne, P.-F. (2013). Principles of E-cadherin supramolecular organization in vivo. *Curr. Biol.* **23**, 2197-2207.
- Vereshchagina, N., Bennett, D., Szoor, B., Kirchner, J., Gross, S., Vissi, E., White-Cooper, H. and Alpey, L. (2004). The essential role of PP1 β in *Drosophila* is to regulate nonmuscle myosin. *Mol. Biol. Cell* **15**, 4395-4405.
- Vincent, J. P. and Lawrence, P. A. (1994). *Drosophila* wingless sustains engrailed expression only in adjoining cells: evidence from mosaic embryos. *Cell* **77**, 909-915.
- Vincent, J.-P. and O'Farrell, P. H. (1992). The state of engrailed expression is not clonally transmitted during early *Drosophila* development. *Cell* **68**, 923-931.
- Wang, Y.-C., Khan, Z., Kaschube, M. and Wieschaus, E. F. (2012). Differential positioning of adherens junctions is associated with initiation of epithelial folding. *Nature* **484**, 390-393.
- Warrington, S. J., Strutt, H. and Strutt, D. (2013). The Frizzled-dependent planar polarity pathway locally promotes E-cadherin turnover via recruitment of RhoGEF2. *Development* **140**, 1045-1054.
- Weng, M. and Wieschaus, E. (2017). Polarity protein Par3/Bazooka follows myosin-dependent junction repositioning. *Dev. Biol.* **422**, 125-134.
- Yamamoto, S., Bayat, V., Bellen, H. J. and Tan, C. (2013). Protein phosphatase 1 β limits ring canal constriction during *Drosophila* germline cyst formation. *PLoS ONE* **8**, e70502.
- Yang, Y., Primrose, D. A., Leung, A. C., Fitzsimmons, R. B., McDermid, M. C., Missellbrook, A., Haskins, J., Smylie, A. L. S. and Hughes, S. C. (2012). The PP1 phosphatase flapwing regulates the activity of Merlin and Moesin in *Drosophila*. *Dev. Biol.* **361**, 412-426.
- Zallen, J. A. and Wieschaus, E. (2004). Patterned gene expression directs bipolar planar polarity in *Drosophila*. *Dev. Cell* **6**, 343-355.
- Zeng, W., Wharton, K. A., Jr, Mack, J. A., Wang, K., Gadabaw, M., Suyama, K., Klein, P. S. and Scott, M. P. (2000). naked cuticle encodes an inducible antagonist of Wnt signalling. *Nature* **403**, 789-795.
- Zhang, L. and Ward, R. E. T. (2011). Distinct tissue distributions and subcellular localizations of differently phosphorylated forms of the myosin regulatory light chain in *Drosophila*. *Gene Expr. Patterns* **11**, 93-104.

Supplementary Materials and Methods

Drosophila strains

The table below lists the alleles used and Table S1 the genotypes for each figure.

Name	Genotype	Origin
yw	y ¹ w ^{67c23}	Bloomington #6599
wg ^{CX4}	wg ^{CX4}	Baker, 1987
enlacZ	en-lacZ	Busturia and Morata, 1988
rokGFP	Ubi-Rok::GFP	Gift from Vincent Mirouse
flwYFP	flwYFP ^{CPTI-002264}	Lowe et al., 2014; Lye et al., 2014
bazGFP	bazGFP ^{CC01941}	Buszczak et al., 2007
prdGal4	prd-Gal4	Bloomington #1947 (Brand & Perrimon 1993)
UASdeGradFP	UAS-deGradFP	Caussinus et al., 2011
armGal4	arm-Gal4	Sanson et al., 1996
UASwg	UAS-wg	Lawrence et al., 1995
MTDGal4	otu-GAL4::VP16, w [*] ; GAL4-nos.NGT; GAL4::VP16-nos.UTR	Bloomington #31777 (Petrella et al., 2007)
UASbazGFP	UASp-baz::GFP	Benton & St Johnston 2003
hh ^{AC}	hh ^{AC}	Lee et al., 1992
sqhGFP40	sqhGFP40 (III)	Royou et al., 2002
eveGFP	eve::EGFP (III)	Venken et al., 2009
Gap43Cherry	GAP43 ^{mem} ::mCherry	Rauzi et al., 2010
baz ^{XR11}	baz ^{XR11}	Kuchinke et al., 1998
nkd ²	nkd ²	Tearle & Nüsslein-Volhard 1987
rhoGal4	rho-Gal4	Ip et. al. 1992
CyO TwistG4 UAS EGFP (CTG)	CyO, P{w[+mC]=GAL4-twi.G}2.2, P{UAS-2xEGFP}AH2.2	Bloomington #6662 (Halfon et al 2002)
CyOwglacZ	CyO-P{en1}wg ^{en1}	Heemskerk & DiNardo 1994
TM6C Twi LacZ (TTLZ)	TM6C, P{w[+mW.hs]=twi-betaGal-1.4t}LS1, Sb[1] Tb[1]	Bloomington #7251 (Seugnet et al 1997)

Immunostainings

Embryonic staging was as in (Hartenstein and Campos-Ortega, 1985). Embryos were collected in a basket from one-hour collections on plates containing apple or grape juice hardened with agar. They were dechorionated by immersion in commercial bleach diluted 1:2 in pure water, for 2 minutes, rinsed, blotted dry and then transferred into heptane. For most experiments, embryos were fixed for 5 minutes in the interface of a 1:1 solution of Heptane:Formaldehyde 37% followed by manual devitelinization in PBS with 0.1% Triton X-100 in (PTX). For staining against phospho-Moesin, 10% trichloroacetic acid in dH₂O was used instead of the formaldehyde, and the embryos fixed on ice for 1 hour. Embryos were then blocked with PTX containing 1% bovine serum albumin (PTB) for 30 minutes, and incubated overnight at 4°C with primary antibodies. They were washed three times for 15 minutes in PTX, then incubated for one hour with secondary antibodies in PTB. They were washed a further three times in PTX, and stored at -20°C in Vectashield (Vector laboratories). When biotin-conjugated secondary antibodies were used an extra step was used. After the second antibody washes the embryos were incubated with streptavidin- conjugated Alexa-405 for 30 minutes before three further washes in PTX, and stored at -20°C in Vectashield.

Antibodies

The following monoclonal primary antibodies were obtained from the Developmental Studies Hybridoma Bank (NICHD and NIH; University of Iowa, Department of Biology, Iowa City): mouse anti-En (4D9; 1:100, Goodman 1989), rat anti-DE-cadherin (DCAD2; 1:50, Takeichi 1994), mouse anti-Dlg (4F3; 1:500, Parnas et al., 2001), rat anti-alpha-catenin (DCAT-1; 1:100, Takeichi 1993), mouse anti-Wingless (4D4; 1:50, Brook & Cohen 1996). Other primary antibodies were: rabbit anti-Baz (1:500; a gift from A. Wodarz), chicken anti- β -Gal (Abcam ab9361; 1:500), mouse anti- β -Gal (Promega Z3781, 1:5000), rabbit anti- β -gal (MP Biomedicals #559761; 1:2500), rabbit anti-Engrailed (Santa Cruz Biotechnology d-300; 1:200), goat anti-GFP-FITC (Abcam ab6556, 1:200), guinea pig anti-Sqh-1P (1:100, a gift from R.E. Ward IV), mouse anti-phospho-Tyrosine (Cell signaling #9411; 1:100), rabbit anti-phospho-Ezrin/Radixin/Moesin (Cell Signalling #3141, 1:200).

Secondary antibodies conjugated to fluorescent dyes were obtained from Jackson ImmunoResearch Laboratories, Invitrogen and Life Technologies. Streptavidin with Alexa Fluor 405 conjugate was from ThermoFisher Scientific. Cell nuclei were stained using Vectashield with DAPI (Vector Laboratories). F-actin was stained using CF594-conjugated phalloidin (Biotium #00045; 1:1,000).

Confocal imaging

Embryos were mounted individually under a coverslip supported by a tape bridge on either side. This flattened the embryos sufficiently so that all cells were roughly in the same z-plane. Embryos were imaged on a Nikon Eclipse TE2000 microscope incorporating a C1 Plus confocal system (Nikon) and images captured using Nikon EZ-C1 software; or, a Leica TCS SP8 confocal microscope and images captured using LAS X software (Leica). Optical z-stacks were acquired with a depth of 0.25 μ m between successive optical z-slices. All embryos were imaged using a violet corrected 60x oil objective lens (NA of 1.4). The gain and offset were optimized for each embryo.

Quantification of enrichment at PSBs

Two stages were used for quantification: stage 10 embryos in all genotypes except for *arm>wg*, where late stage 9 embryos were analyzed to avoid too much folding at ectopic boundaries. Quantifications were done in maximum intensity projections, which were made from the minimum number of z-slices needed to contain all the adherens junction signal. The adherens junctions were labelled by staining for either E-Cadherin or phospho-Tyrosin. Cortical signal of different proteins was quantified on line traces that went over cell interfaces. The position of the PSB was identified by co-staining with anti-En or anti-Wg, except for *wg^{CX4}* embryos in which these markers are gradually lost; in this case, an *enlacZ* transgene was used and staining with anti- β Gal showed the PSB location (β Gal protein has longer perdurance than En protein in embryos). The lines were manually traced by using the FIJI plugin Simple Neurite Tracer (Longair et al., 2011) or the ImageJ plugin NeuronJ (Meijering et al., 2004) based on membrane marker stainings and avoiding dividing cells. Average fluorescence intensity was quantified for 3-pixel wide line traces using ImageJ or FIJI (Schneider et al, 2012; Schindelin et al, 2012). We used the image-wide modal pixel intensity as an approximation of the average background fluorescence. The modal pixel intensity was then subtracted from all pixels to remove background fluorescence from the signal. PSB and Ectopic Boundary interface fluorescence intensity was then normalised to En interface fluorescence intensity for each PSB quantification (Example in Figure 1 D'', G''), with the exception of Baz, for which it was normalized to DV tracks outside the Engrailed domain (Example in Figure 1E'', H''). This is because contrarily to the other proteins we looked at, Baz shows a very weak remaining planar polarity at stage 10, in particular in the Engrailed domain. Statistics were performed in Prism (GraphPad). Pilot experiments were used to establish that $n \approx 20$ PSBs was appropriate for the detection of enrichments or depletions. Data from all quantifications are reported as mean \pm 95% confidence intervals. Results were considered significant when $p < 0.05$ (* when $p < 0.05$, ** when $p < 0.01$, *** when $p < 0.001$, **** when $p < 0.0001$).

3D image segmentation, quantification of cell areas, AJ position and index of straightness

Wildtype and *arm>wg* stage 10 embryos were stained with Engrailed and E-Cadherin antibodies as well as CF594-Phalloidin to mark PSBs, adherens junctions and actin respectively. Then, embryos were mounted under a coverslip suspended by a two-layer thick tape bridge on either side. The samples were imaged on a Leica TCS SP8 confocal microscope (CAIC, University of Cambridge). Optical z-stacks were acquired with a depth of 0.33 μm between successive optical z-slices, which is the optimal z interval thickness of the 63X objective used. The gain and offset were optimized for each embryo. Fluorescence images were denoised (Boulanger et al., 2010) and segmented using Real-time Accurate Cell-shape Extractor (Stegmaier et al., 2016). Cell top was detected by the apical medial actin enrichment while cortical actin decorated cell contour. Segmented images were used in ImageJ to manually select cells of different populations (Control, PSB and ectopic PSBs: ECT) in wildtype and *arm>wg* embryos. Selected cells were saved as region of interests and used to quantify cell area per stack and 3D render. Custom written MATLAB scripts computed cell areas for the chosen cells in each plane of the stack.

For the adherens junctions apico-basal position, analysis contours were generated as described above for the quantification of protein enrichments at PSBs and saved as 2D binary masks. The cell walls corresponding to the regions of interest were determined by propagating these contours as open snakes on the cortical Phalloidin channel intensities (Shemesh and Ben-Shahar, 2001). These cell walls were then used to quantify the distance between the adherens junctions (E-cadherin) and the top of the cell, detected by medial actin (Phalloidin). The positions of the adherens junctions were given by the maxima of E-cadherin channel values in z direction along the wall. An estimate of the top of the cell was obtained by segmenting the Phalloidin channel stack in 2D (xz direction) via robust statistics based thresholding of the wavelet coefficients of the image. 2D projections of intensities in the E-cadherin and Phalloidin channel (across the width of the bounding box for each input contour) were saved as a mean of quality control by visual inspection. The distance between adherens junctions and the closest point of the cell top was computed taking into account voxel anisotropy. Finally, as a post-processing step of removing outliers, the highest 10% of distances were discarded for each region.

The index of straightness (IS, (Monier et al., 2010) was computed for each propagated contour in each plane of the 3D stack over a depth of 5 microns (starting from 0.6 microns above the adherens junctions). It is calculated as representing the percentage of curve length exceeding the length of the straight line joining the curve's endpoints:

$$\text{IS} = (\text{length of curve} / \text{distance between the two endpoints of the curve} - 1) * 100$$

Scanning Electron microscopy

Embryos were fixed for 5 minutes in Heptane:Formaldehyde 37% (1:1) and devitellinised with Heptane:Methanol (1:1). Then, they were re-fixed immediately in 2% Glutaraldehyde, 2% Formaldehyde, 0.05M Sodium Cacodylate pH 7.4 and 2mmol/L Calcium Chloride overnight. Once rinsed twice in deionised water, embryos were treated with 1% osmium ferricyanide for 3 days. After that they were rinsed four times in deionised water, dehydrated to 100% ethanol and dried by either critical point drying, or drying from hexamethyldisilazane (HMDS). Where HMDS was used, embryos were transferred into 1:1 HMDS:ethanol for 10 minute, then HMDS for 10 minutes twice, and left to dry. Dry embryos were mounted on carbon tabs on 12.5 mm Cambridge stubs and sputter coated with 50nm of gold. Images were taken in a FEI XL30 FEG scanning electron microscope operated at 5 kV.

Y-27632 Rho kinase inhibitor injections

Early stage 9 *arm>wg* embryos were injected through the posterior into the yolk at room temperature with 1 mM Y27632 in dH_2O , and dH_2O in control experiments. Embryos were aged for 45 minutes at 25°C, then fixed in 8% formaldehyde over heptane for 20

minutes. They were rinsed with PBS, manually devitellinised by nicking with a needle, and then fixed for SEM as above.

Live Imaging

Dechorionated embryos were transferred into halocarbon oil (Votalef PCTFE, Arkema), mounted ventral side up on stretched oxygen-permeable membrane, and covered with a coverslip supported by a bridge of a single coverslip on either side. Timelapse imaging was carried out on a Nikon Eclipse E1000 equipped with a spinning disk unit (Yokogawa CSU10), laser module with 491nm and 561nm excitation (Spectral Applied Research LMM2), and a C9100-13 EM-CCD camera (Hamamatsu). Z-stacks were acquired with an interval of 0.7µm or 1µm. Images were captured using Volocity software (PerkinElmer). Where multiple images were stitched together (Fig S4C), the FIJI plugin Grid/collection Stitching was used (Preibisch et al., 2009).

Laser ablations and analysis of recoil velocities

Laser ablation experiments were carried out on a TriM Scope II Upright 2-photon Scanning Fluorescence Microscope controlled by Inspector Pro software (LaVision Biotec) using a tuneable near-infrared (NIR) laser source delivering 120 femtosecond pulses with a repetition rate of 80 MHz (Insight DeepSee, Spectra-Physics). The laser was tuned to 927nm, with power ranging between 1.40-1.70 W. The maximum laser power allowed to reach the sample was set to 220 mW and an Electro-Optical Modulator (EOM) was used to allow microsecond switching between imaging and treatment laser powers. The laser light was focused by a 25x, 1.05 Numerical Aperture (NA) water immersion objective lens with a 2mm working distance (XLPLN25XWMP2, Olympus). Images were collected every 0.731 ms for 5 frames before the ablation and 60 frames after the ablation.

Ablations were performed during image acquisition (with a dwell time of 9.27 µsec per pixel), with the laser power switching between treatment and imaging powers as the laser was raster scanned across the sample. Targeted line ablations of about 2 µm length were performed at the centre of junctions on the PS boundary or on control, non boundary dorso-ventral (DV) oriented or antero-posterior (AP) oriented junctions, using a treatment power of 220 mW. 20-25 ablations per condition per genotype were carried out, 2-4 ablations per embryo.

To analyse recoil velocities, a kymograph spanning the ablated region was extracted using the dynamic reslice function in Fiji, and the distance between the two ends of the cut was measured up to 30 seconds after ablation. Linear regression was performed on the first 5 timepoints after ablation and the slope of the regressed line was used to measure the recoil velocity of the cut ends.

References:

- Baker, N.E. (1987). Molecular cloning of sequences from wingless a segment polarity gene in *Drosophila* the spatial distribution of a transcript in embryos. *EMBO J.* 6(6): 1765--1774.
- Benton, R. & St. Johnston, D. (2003). A conserved oligomerization domain in *Drosophila* Bazooka/PAR-3 is important for apical localization and epithelial polarity. *Curr. Biol.* 13(15): 1330--1334.
- Boulanger, J., Kervrann, C., Bouthemmy, P., Elbau, P., Sibarita, J. B. and Salamero, J. (2010). Patch-based nonlocal functional for denoising fluorescence microscopy image sequences. *IEEE transactions on medical imaging* 29, 442-454.
- Brand, A.H., Perrimon, N. (1993). Targeted gene expression as a means of altering cell fates

and generating dominant phenotypes. *Development* 118(2): 401--415.

Brook W.J. & Cohen SM. (1996). Antagonistic interactions between wingless and decapentaplegic responsible for dorsal-ventral pattern in the *Drosophila* Leg. *Science* 273(5280): 1373-7.

Busturia, A., Morata, G. (1988). Ectopic expression of homeotic genes caused by the elimination of the Polycomb gene in *Drosophila* imaginal epidermis. *Development* 104: 713-720.

Buszczak, M., et al. (2007). The Carnegie protein trap library: A versatile tool for *Drosophila* developmental studies. *Genetics* 175(3): 1505--1531.

Caussinus, E., et al. (2011). Fluorescent fusion protein knockout mediated by anti-GFP nanobody. *Nat. Struct. Mol. Biol.* 19(1): 117--121.

Goodman CS. (1989). Expression of engrailed proteins in arthropods, annelids, and chordates. *Cell* 58(5): 955-68.

Halfon, M.S., et al. (2002). New fluorescent protein reporters for use with the *Drosophila* Gal4 expression system and for vital detection of balancer chromosomes. *genesis* 34(1-2): 135--138.

Hartenstein, V. and Campos-Ortega, J. A. (1985). Fate-mapping in wild-type *Drosophila melanogaster*. 1. The spatio-temporal pattern of embryonic cell divisions. *Roux's Arch. Dev. Biol.* 194, 181-195.

Heemskerk, J. & DiNardo, S. (1994). *Drosophila* hedgehog acts as a morphogen in cellular patterning. *Cell* 76(3): 449--460.

Ip, T.Y., et al. (1992). The dorsal gradient morphogen regulates stripes of rhomboid expression in the presumptive neuroectoderm of the *Drosophila* embryo. *Genes Dev.* 6, 1728-1739.

Kuchinke, U., et al. (1998). Control of spindle orientation in *Drosophila* by the Par-3-related PDZ-domain protein Bazooka. *Curr. Biol.* 8(25): 1357--1365.

Lawrence, P.A., et al. (1995). Segmental patterning of heart precursors in *Drosophila*. *Development* 121(12): 4303--4308.

Lee, J.J., et al. (1992). Secretion and localized transcription suggest a role in positional signaling for products of the segmentation gene hedgehog. *Cell* 71(): 33--50.

Longair, M. H., Baker, D. A. and Armstrong, J. D. (2011). Simple Neurite Tracer: open source software for reconstruction, visualization and analysis of neuronal processes. *Bioinformatics* 27, 2453--2454.

Lowe, N., et al. (2014). Analysis of the expression patterns, subcellular localisations and interaction partners of *Drosophila* proteins using a pigP protein trap library. *Development* 141(20): 3994--4005.

Lye, C.M., et al. (2014). Subcellular localisations of the CPTI collection of YFP-tagged proteins in *Drosophila* embryos. *Development* 141(20): 4006--4017.

- Meijering E., et al. (2004). Design and Validation of a Tool for Neurite Tracing and Analysis in Fluorescence Microscopy. *Cytometry A*. 58(2):167-76.
- Monier, B., Pelissier-Monier, A., Brand, A. H. and Sanson, B. (2010). An actomyosin-based barrier inhibits cell mixing at compartmental boundaries in *Drosophila* embryos. *Nat Cell Biol* 12, 60-65.
- Parnas D, Haghighi AP, Fetter RD, Kim SW, Goodman CS. (2001). Regulation of postsynaptic structure and protein localization by the Rho-type guanine nucleotide exchange factor dPix. *Neuron*. 32(3):415-24.
- Petrella, L.N., et al. (2007). The Ovhts polypeptide is cleaved to produce fusome and ring canal proteins required for *Drosophila* oogenesis. *Development* 134(4): 703--712.
- Preibisch S., et al. (2009). Globally optimal stitching of tiled 3D microscopic image acquisitions. *Bioinformatics* 25(11): 1463--1465.
- Rauzi, M., et al. (2010). Planar polarized actomyosin contractile flows control epithelial junction remodelling. *Nature* 468(7327): 1110--1114.
- Royou, A., et al. (2002). Cortical recruitment of nonmuscle myosin II in early syncytial *Drosophila* embryos: its role in nuclear axial expansion and its regulation by Cdc2 activity. *J. Cell Biol.* 158(1): 127--137.
- Sanson, B., et al. (1996). Uncoupling cadherin-based adhesion from wingless signalling in *Drosophila*. *Nature* 383(6601): 627--630.
- Schindelin, J., et al. (2012). Fiji: an open-source platform for biological-image analysis. *Nature methods* 9(7): 676-682,
- Schneider, C.A., et al. (2012). NIH Image to ImageJ: 25 years of image analysis. *Nature methods* 9(7): 671-675
- Seugnet, L., et al. (1997). Transcriptional regulation of Notch and Delta: requirement for neuroblast segregation in *Drosophila*. *Development* 124(10): 2015--2025.
- Shemesh M. & Ben-Shahar O. (2011) Free Boundary Conditions Active Contours with Applications for Vision. In: Bebis G. et al. (eds) *Advances in Visual Computing*. ISVC 2011. *Lecture Notes in Computer Science*, vol 6938. Springer, Berlin, Heidelberg
- Stegmaier J, et al. (2016). Real-Time Three-Dimensional Cell Segmentation in Large-Scale Microscopy Data of Developing Embryos. *Dev Cell*. 36(2):225-40.
- Takeichi M. (1993). Identification of a *Drosophila* homologue of alpha-catenin and its association with the armadillo protein. *The Journal of cell biology* 121(5): 1133-40.
- Takeichi M. (1994). A *Drosophila* homolog of cadherin associated with armadillo and essential for embryonic cell-cell adhesion. *Developmental biology* 165(2): 716-26.
- Tearle, R.G. & Nusslein-Volhard, C. (1987). Tübingen mutants and stock list. *D. I. S.* 66(): 209--269.
- Venken, K.J.T., et al. (2009). Versatile P[acman] BAC libraries for transgenesis studies in *Drosophila melanogaster*. *Nat. Methods* 6(6): 431--434.

Figure	Panel	Parental genotype(s)	Embryo genotype
1	A, D-D'', E-E'', I	yw	yw
1	B, H-H''	wg ^{CX4} /CTG	wg ^{CX4} /wg ^{CX4}
1	G-G'', I	wg ^{CX4} , en-lacZ/CTG x wg ^{CX4} /CTG	wg ^{CX4} , en-lacZ/wg ^{CX4}
1	I	Ubi-Rok::GFP/TM3Sb	Ubi-Rok::GFP/TM3Sb
1	I	flwYFP	flwYFP
1	I	wg ^{CX4} /CTG; Ubi-Rok::GFP/TTLZ x wg ^{CX4} , en-lacZ/CTG	wg ^{CX4} , en-lacZ/wg ^{CX4} ; Ubi-Rok::GFP/+
1	I	♂flwYFP; wg ^{CX4} /CTG x ♂ wg ^{CX4} , en-lacZ/CTG	flwYFP/+ ; wg ^{CX4} /wg ^{CX4}
1	J, J', K	w;; sqhGFP40	w;; sqhGFP40
1	L	wg ^{CX4} /CTG; sqhGFP40	wg ^{CX4} /wg ^{CX4} ; sqhGFP40
2	A, B-B'', D, D', E, F, H-H''	flwYFP;; prdGal4/TTLZ x flwYFP;; UAS-deGradFP/UAS-deGradFP	flwYFP;; prdGal4/UAS-deGradFP
2	C, E	flwYFP;; prdGal4/TTLZ x flwYFP;; UAS-deGradFP/UAS-deGradFP	flwYFP;; TTLZ/UAS-deGradFP
3	D-D'', E, H-H'', J-J', K-K'	♂armGal4 x ♂ UAS-wg	armGal4/+; UAS-wg/+
3	I	yw	yw
3	E	♂armGal4/+; Ubi-Rok::GFP/+ x ♂ UAS-wg	armGal4/+; Ubi-Rok::GFP/UAS-wg
3	E	flwYFP; armGal4 x flwYFP;; UAS-wg	flwYFP; armGal4/+; UAS-wg/+
3	F	♂armGal4; sqhGFP40 x ♂ UAS-wg	armGal4/+; UAS-wg/sqhGFP40
4	B-B', D-D'', E, F	♂MTDGal4/UAS-bazGFP x ♂ UAS-bazGFP	UAS-bazGFP/(UAS-bazGFP or MTDGal4)
4	C	♂MTDGal4/UAS-bazGFP; sqhGFP40 x ♂ UAS-bazGFP; sqhGFP40	UAS-bazGFP/(UAS-bazGFP or MTDGal4); sqhGFP40/(sqhGFP40 or MTDGal4)
4	E, F	yw	yw
5	B, D, E	♂armGal4 x ♂ UAS-wg	armGal4/+; UAS-wg/+
5	C, D, E	♂armGal4; hh ^{AC} /TTLZ x ♂ UAS-wg, hh ^{AC} /TTLZ	armGal4/UAS-wg ; hh ^{AC} /hh ^{AC}
6	A-A'''	sqh ^{AX3} ; sqhGFP42; Gap43-mCherry/TM6B	sqh ^{AX3} ; sqhGFP42; Gap43-mCherry/TM6B
6	B-B'''	♂armGal4/CTG; Gap43-mCherry, eve-GFP/TM6B x ♂ UAS-wg	armGal4/+; Gap43-mCherry, eve-GFP/UAS-wg
7	A-A', C, E, G, I	yw	yw
7	B-B', D, F, H, J	♂armGal4 x ♂ UAS-wg	armGal4/+; UAS-wg/+
S1	A-A''	yw	yw

S1	B-B''	<i>Ubi-Rok::GFP/TM3Sb</i>	<i>Ubi-Rok::GFP/TM3Sb</i>
S1	C-C''	<i>flwYFP</i>	<i>flwYFP</i>
S1	D-D'	<i>w;; sqhGFP40</i>	<i>w;; sqhGFP40</i>
S1	E-E'	<i>wg^{CX4}/CTG; sqhGFP40</i>	<i>wg^{CX4}/wg^{CX4}; sqhGFP40</i>
S2	A-A'', B-B'', C-C''	<i>flwYFP</i>	<i>flwYFP</i>
S2	D	<i>flwYFP;; prdGal4/TTLZ</i> <i>x flwYFP;; UAS-deGradFP/UAS-deGradFP</i>	<i>flwYFP;; prdGal4/UAS-deGradFP</i>
S3	A-A''	<i>♂armGal4 x ♂ UAS-wg</i>	<i>armGal4/+; UAS-wg/+</i>
S3	B-B'	<i>♂armGal4; sqhGFP40 x ♂ UAS-wg</i>	<i>armGal4/+; UAS-wg/sqhGFP40</i>
S3	D-D', E-E''	<i>♂rhoGal4 x ♂ UAS-wg</i>	<i>rhoGal4/+; UAS-wg/+</i>
S3	G-G', H-H''	<i>nkd²/TTLZ</i>	<i>nkd²/nkd²</i>
S4	A	<i>yw</i>	<i>yw</i>
S4	A	<i>♂MTDGal4/UAS-bazGFP x ♂ UAS-bazGFP</i>	<i>UAS-bazGFP/(UAS-bazGFP or MTDGal4)</i>
S4	B-B'	<i>♂MTDGal4/UAS-bazGFP; sqhGFP40</i> <i>x ♂ UAS-bazGFP; sqhGFP40</i>	<i>UAS-bazGFP/(UAS-bazGFP or MTDGal4);</i> <i>sqhGFP40/(sqhGFP40 or MTDGal4)</i>
S4	C	<i>♂bazGFP;; prdGal4/TM6B x ♂ bazGFP; UAS-deGradFP</i>	<i>bazGFP/bazGFP; UAS-deGradFP/+; prdGal4/+</i>
S4	D	<i>♂bazGFP/baz^{XR11}; armGal4 x ♂ bazGFP; UAS-</i> <i>deGradFP/CyOwglacZ; UAS-wg/TM6B</i>	<i>bazGFP/baz^{XR11}; armGal4/UAS-deGradFP; UAS-wg/+</i>
S4	E	<i>♂bazGFP; armGal4 x ♂ bazGFP; UAS-deGradFP/CyOwglacZ;</i> <i>UAS-wg/TM6B</i>	<i>bazGFP/bazGFP; armGal4/UAS-deGradFP; UAS-wg/+</i>
S5	A, C-C'', D-D''	<i>yw</i>	<i>yw</i>
S5	B, E-E'', F-F''	<i>♂armGal4 x ♂ UAS-wg</i>	<i>armGal4/+; UAS-wg/+</i>

Table S1: List of genotypes used in figures

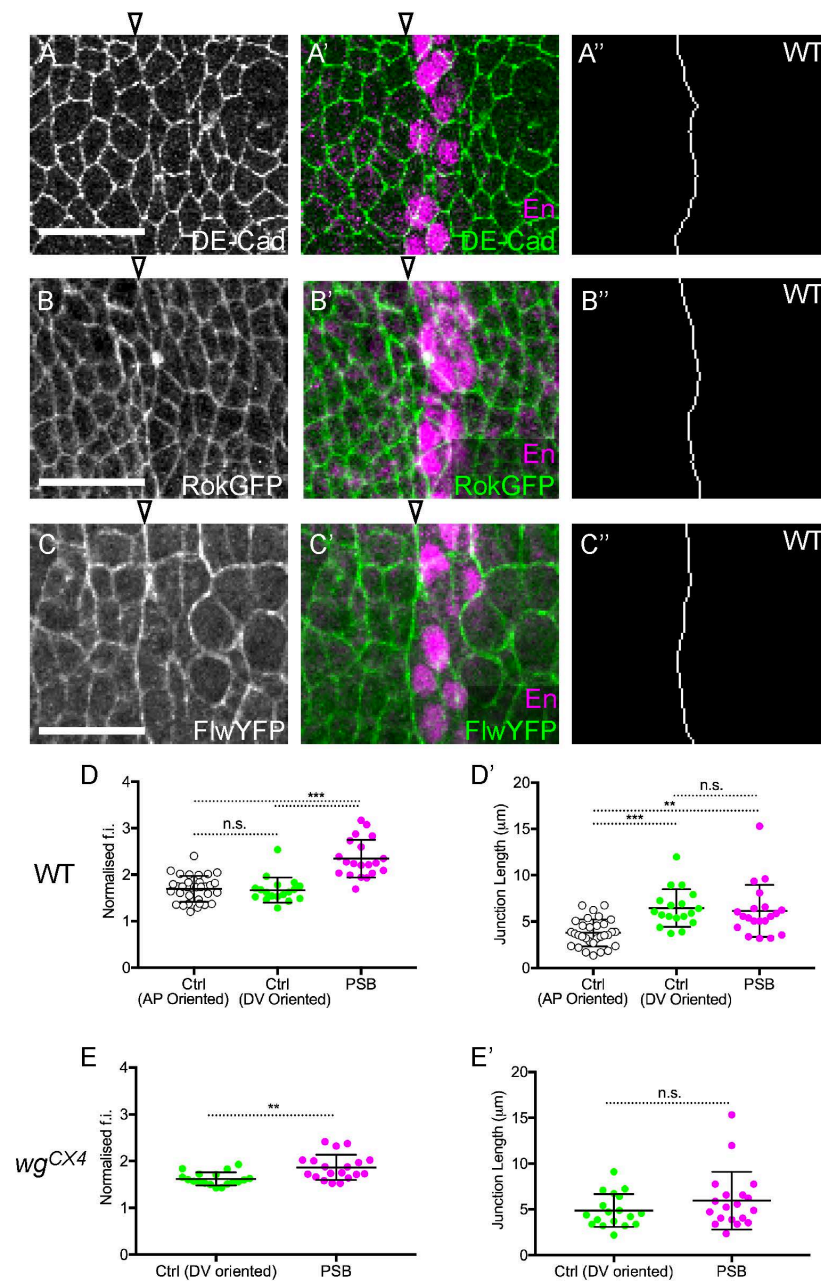


Figure S1: Planar polarities and actomyosin contractility at the PSBs. (A-C'') Example immunostainings used for quantification in Fig. 1I. (A,B,C) Immunostaining against each marker; (A',B',C') merged with Engrailed marker staining to locate the PSBs (open arrowheads). (A'',B'',C'') Tracings along PSB cell-cell junctions. (D-E') Controls for laser ablations shown in Fig. 1J-L: Myosin II intensity and junction length. (D,E) Quantification of Myosin-II fluorescence intensity (f.i.) using the Sqh-GFP signal at ablated PSB and control junctions in (D) wildtype and (E) *wg^{CX4}* embryos. Comparisons in (D) from a Kruskal-Wallis Test: AP controls vs. DV controls: $p > 0.999$, n.s.; AP controls vs. PSBs: $p < 0.0001$ ****; DV controls vs. PSBs: $p < 0.0001$ ****. Comparison in (E) from a t-test: $p = 0.0015$ **. (D',E') Length of the ablated PSB and control cell-cell junctions. DV-oriented junctions (PSB and control) are longer than AP-oriented junctions as cells tend to be DV-elongated at this stage. This length difference does not appear to affect recoil speed (see Fig. 1K). Error bars show mean \pm s.d. Comparisons in (D') from a Kruskal-Wallis Test: AP controls vs. DV controls: $p < 0.0001$ ****; AP controls vs. PSBs: $p = 0.0016$ **; DV controls vs. PSBs: $p > 0.999$, n.s. Comparison in (E') from a Mann-Whitney test: $p = 0.316$, n.s.

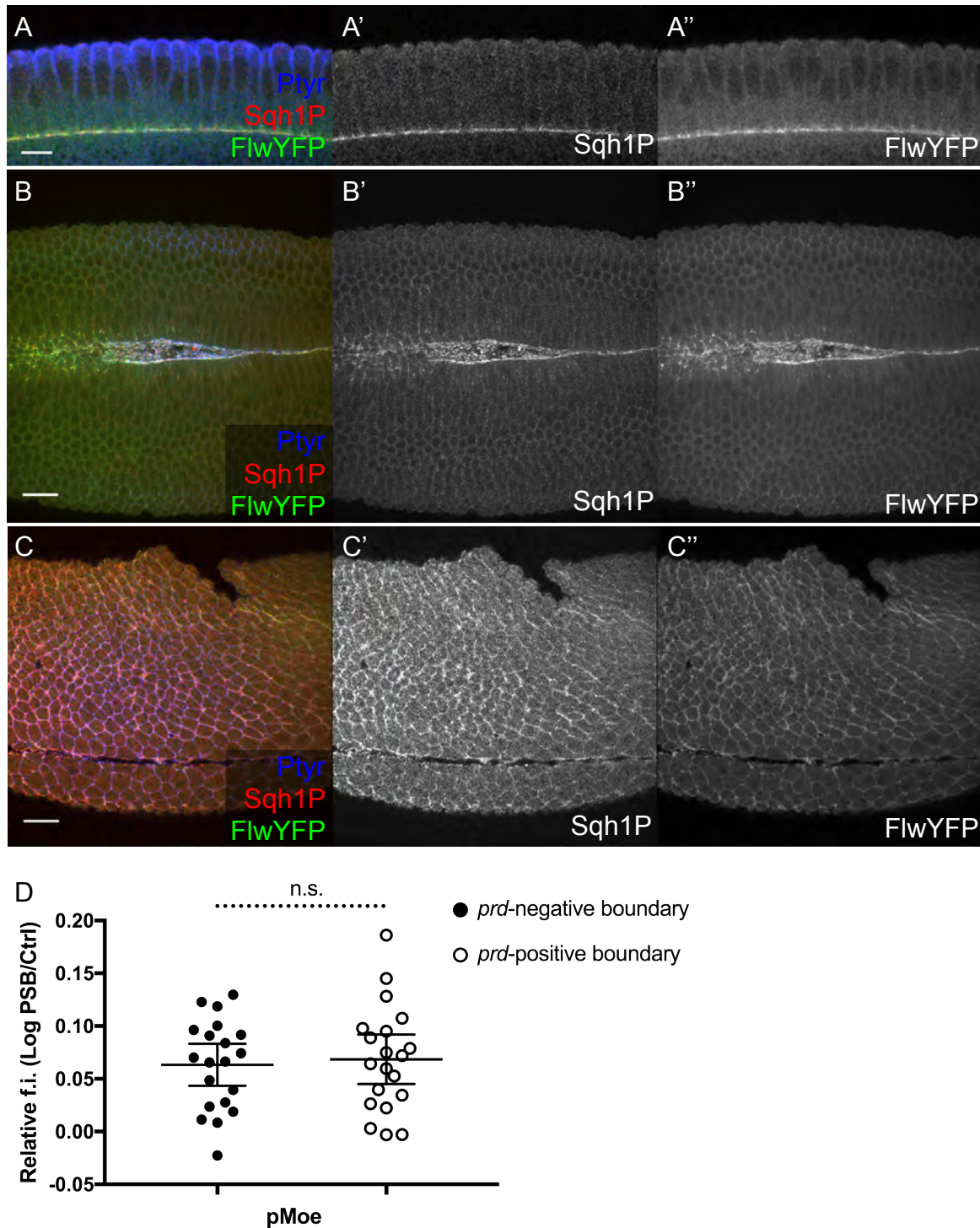


Figure S2: Localisation of Flapwing in early embryos and pMoesin quantification at Flapwing-depleted parasegment boundaries. (A-C'') Immunostainings against Flapwing-YFP (Flw-YFP) and monophosphorylated Sqh (Sqh1P) in early embryos. (A-A'') Sagittal view of an embryo during cellularisation. (B-B'') View of the invaginating mesoderm during gastrulation. (C-C'') View of the extending germband of a stage 7 embryo. (A'',B'',C'') anti-GFP staining to label Flw-YFP; (A',B',C') Sqh1P staining; (A,B,C) merged channels with the adherens junction marker phosphoTyrosine (pTyr). Scale bars: 20 μm. (D) Quantification of fluorescence intensity (f.i.) of phospho-Moesin (pMoe) along PSBs in deGradFP-expressing and -non-expressing domains (prd-Gal4 positive or negative), relative to control cell interfaces, as log₁₀. n=20 PSBs for both types. Error bars show mean±95% c.i. Comparison from a Mann-Whitney test: p=0.925, n.s.

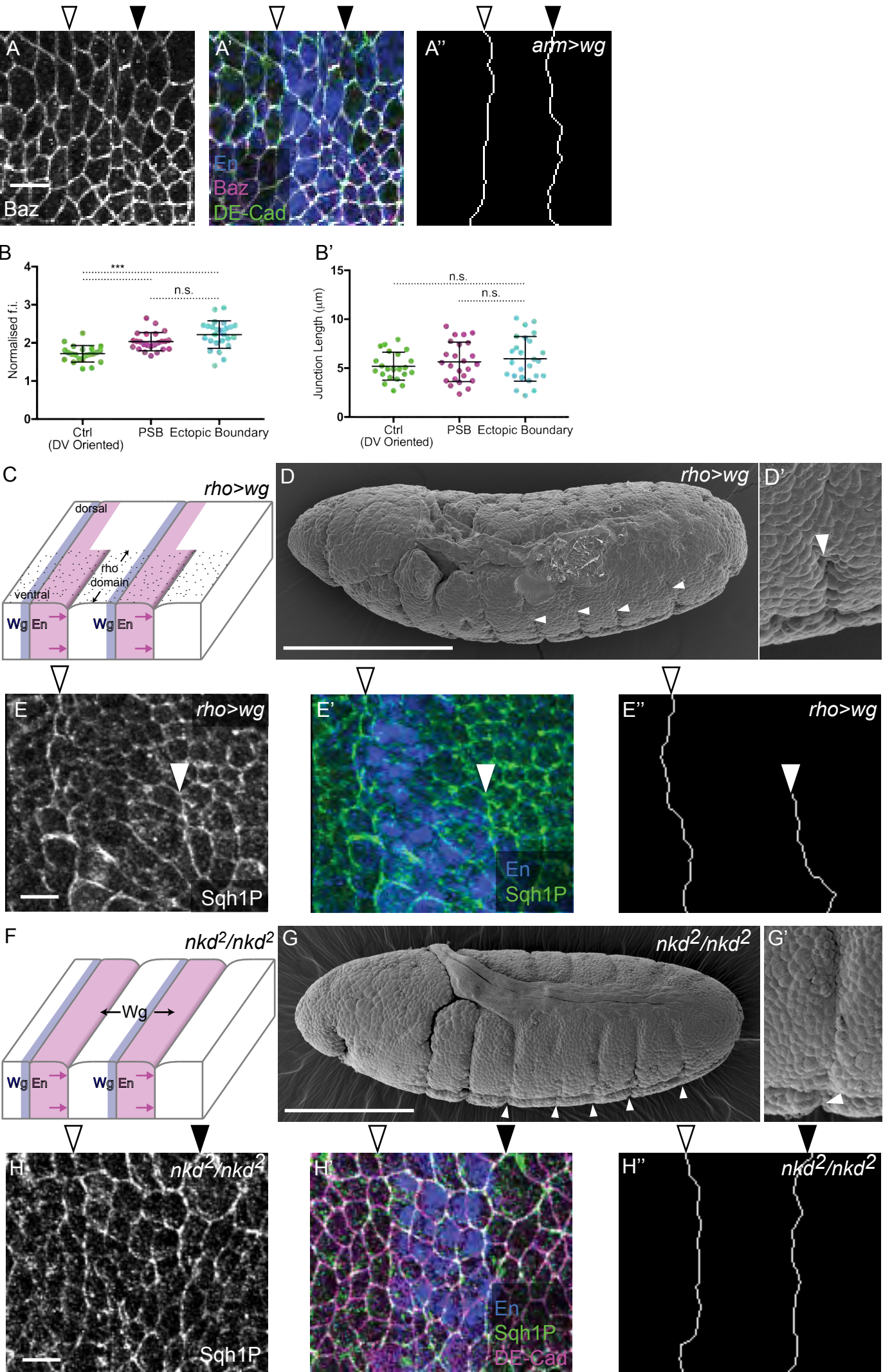


Figure S3: Ectopic PSBs in embryos ectopically expressing Wingless. (A-A') Immunostaining of *arm>wg* stage 10 embryo against (A) Bazooka (Baz), (A') merged with Engrailed (En) and E-Cadherin (DE-Cad). (A'') Tracings of cell-cell contacts at endogenous and ectopic PSBs. Scale bar: 10 μ m. (B,B') Controls for ablations shown in Fig. 3F: Myosin-II intensity and junction length. (B) Quantification of Myosin-II fluorescence intensity (f.i.) using the Sqh-GFP signal at ablated control, endogenous PSB and ectopic PSB junctions. Error bars show mean \pm s.d. Comparisons from a one-way ANOVA: DV controls vs. PSBs: $p=0.0009^{***}$; DV controls vs. ectopics: $p<0.0001^{****}$; PSBs vs. ectopics: $p=0.0615$, n.s. (B') Junction lengths of the same ablated junctions. Error bars show mean \pm s.d. Comparisons from a one-way ANOVA: DV controls vs. PSBs: $p=0.661$, n.s.; PSBs vs. ectopics: $p=0.322$, n.s. (C-E'') Formation of ectopic PSBs in embryos expressing *UAS-wg* under the control of *rho-Gal4* (*rho>wg*). (C) Diagram showing position of deep folds at ventral ectopic PSBs in *rho>wg* embryos. (D) SEM showing short ventral folds at ectopic PSBs in *rho>wg* embryos (close-up in D'). Scale bar: 100 μ m. (E,E') *rho>wg* embryos immunostained against (E) Sqh1P and (E') merged with Engrailed (En). (E'') Tracings of the endogenous and ectopic PSBs. Scale bar: 10 μ m. (F-H'') Formation of ectopic PSBs in *nkd²* null mutant embryos. (F) Diagram showing position of deep folds at ectopic PSBs in *nkd²* embryos. (G) SEM showing deep folds at ectopic PSBs in *nkd²* embryos (close-up in G'). Scale bar: 100 μ m. (H,H') *nkd²* embryos immunostained against (H) Sqh1P and (H') merged with En and DE-Cad. (H'') Tracings of endogenous and ectopic PSBs. Scale bar: 10 μ m. Open arrowheads depict endogenous PSBs; filled arrowheads ectopic PSBs.

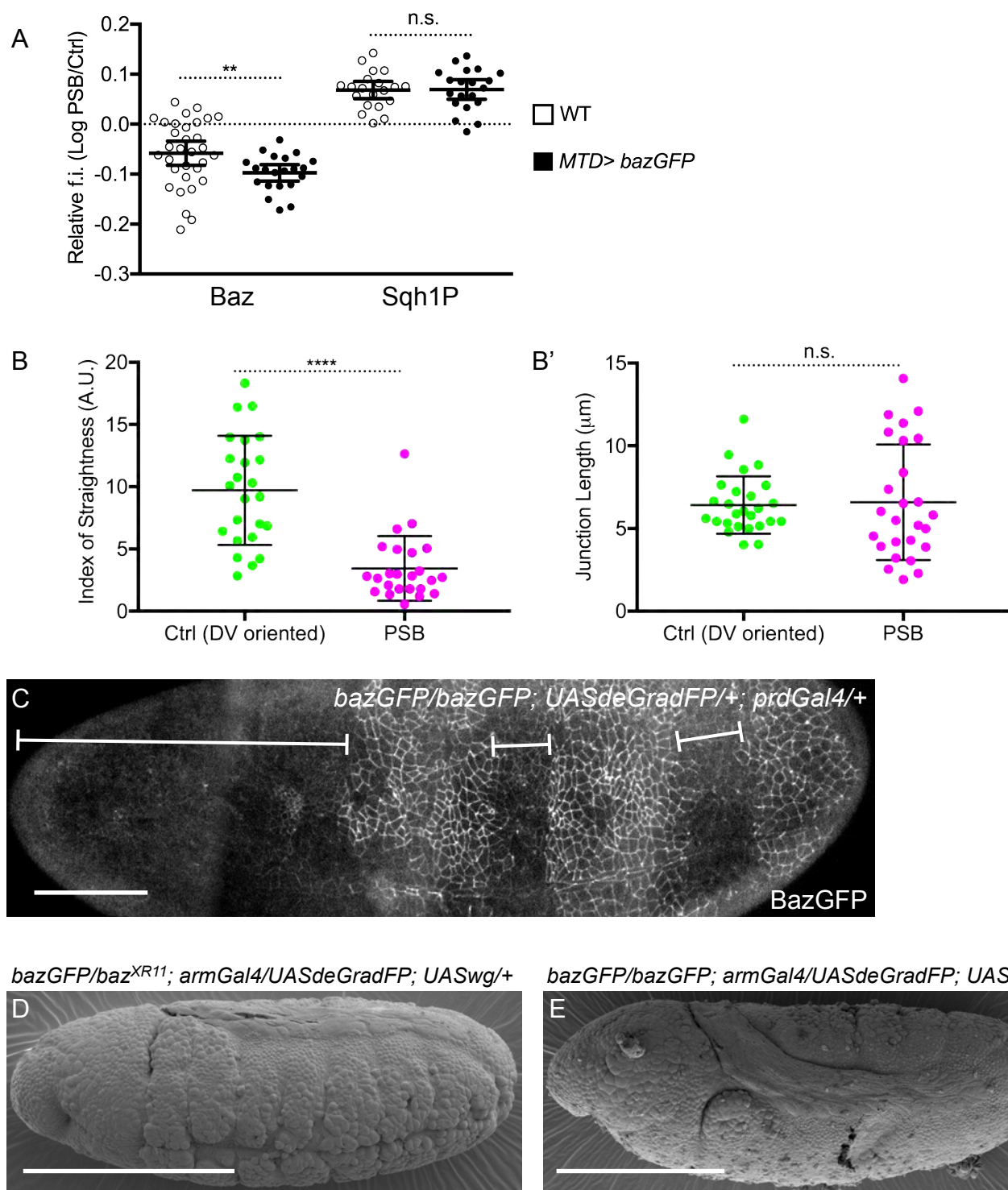


Figure S4: Planar polarities and actomyosin contractility at the PSBs in Bazooka-overexpressing embryos. (A) Quantification of fluorescence intensity (f.i.) of Baz and Sqh1P at PSBs relative to control DV-oriented interfaces in wildtype (open circles) and *MTD>bazGFP* (filled circles) stage 10 embryos, as \log_{10} . Error bars show mean \pm 95% c.i. Baz in WT: n=32 boundaries; Baz in *MTD>bazGFP*: n=21; Sqh1P in WT: n=20; Sqh1P in *MTD>bazGFP*: n=20. Comparisons from t-tests: Baz: $p=0.0081^{**}$; Sqh1P: $p=0.933$, n.s. (B,B') Index of straightness and junction length measurements for the laser ablations in *MTD>bazGFP* embryos (see Fig. 4C). (B) Quantification of index of straightness, a proxy for junctional tension. For both DV controls and PSBs n=24. Comparison from a Mann-Whitney test: $p<0.0001^{****}$. (B') Lengths of ablated junctions at PSBs and DV controls. For both DV controls and PSBs n=26. Comparison from a Mann-Whitney test: $p=0.528$, n.s. Error bars show mean \pm s.d. (C) Ventral view of a live stage 10 embryo expressing BazGFP, with degradation of GFP-tagged protein due to expression of deGradFP under the control of *prdGal4*. Brackets show loss of BazGFP signal in *prd-Gal4* domains. Scale bar: 50 μ m. (D,E) SEM of embryos depleted for Baz by deGradFP in *arm>wg* embryos. Scale bars: 100 μ m. (D) A sensitized *baz* genetic background with *bazGFP/baz^{XRII}* in addition to deGradFP under the control of *armGal4* causes loss of epithelial integrity, especially ventrally (cells are rounding up), but deep folds remain. n=18 embryos. (E) In an embryo with *bazGFP/bazGFP* with deGradFP under the control of *armGal4*, loss of epithelial integrity is less pronounced. n=6 embryos.

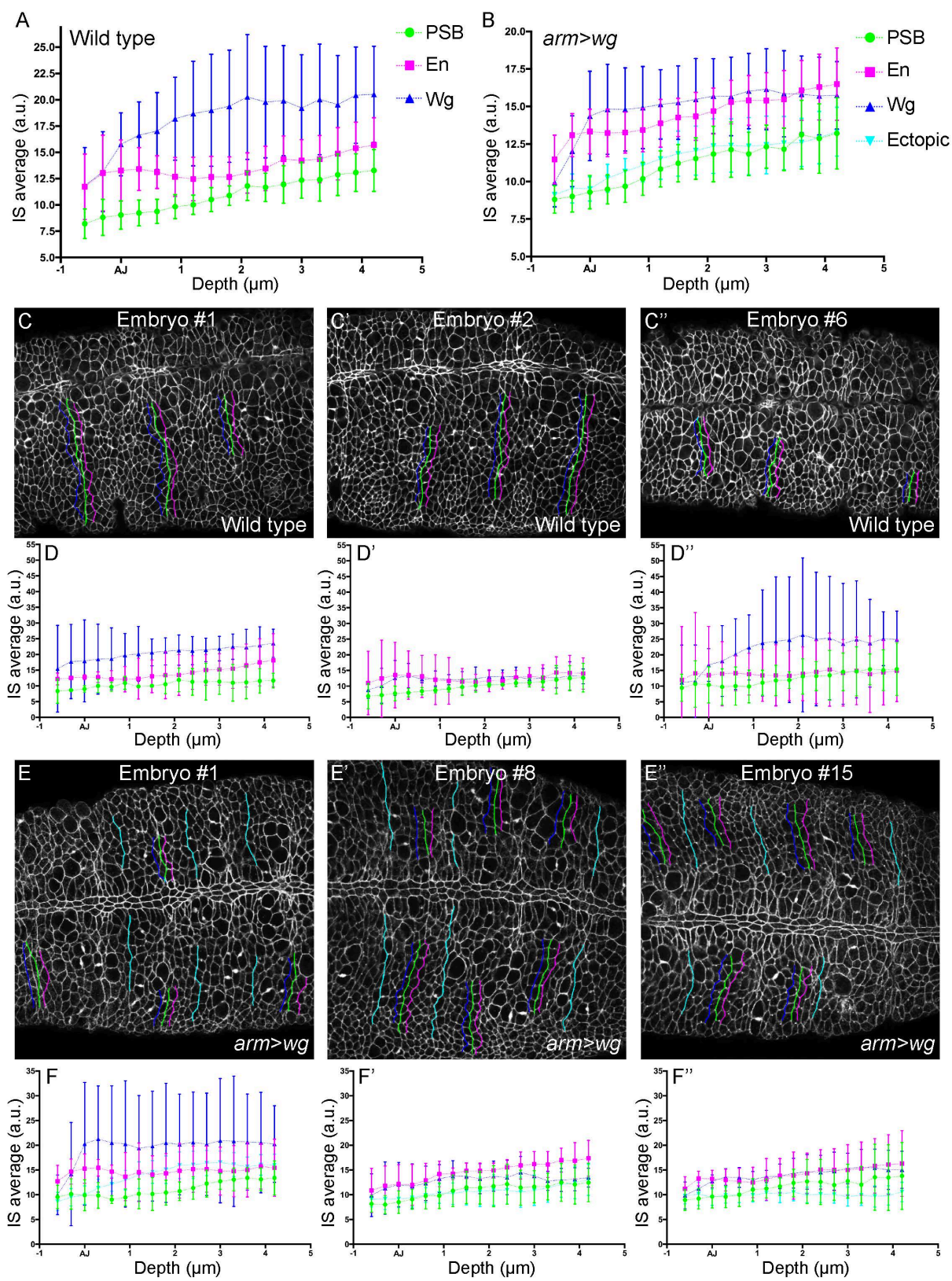
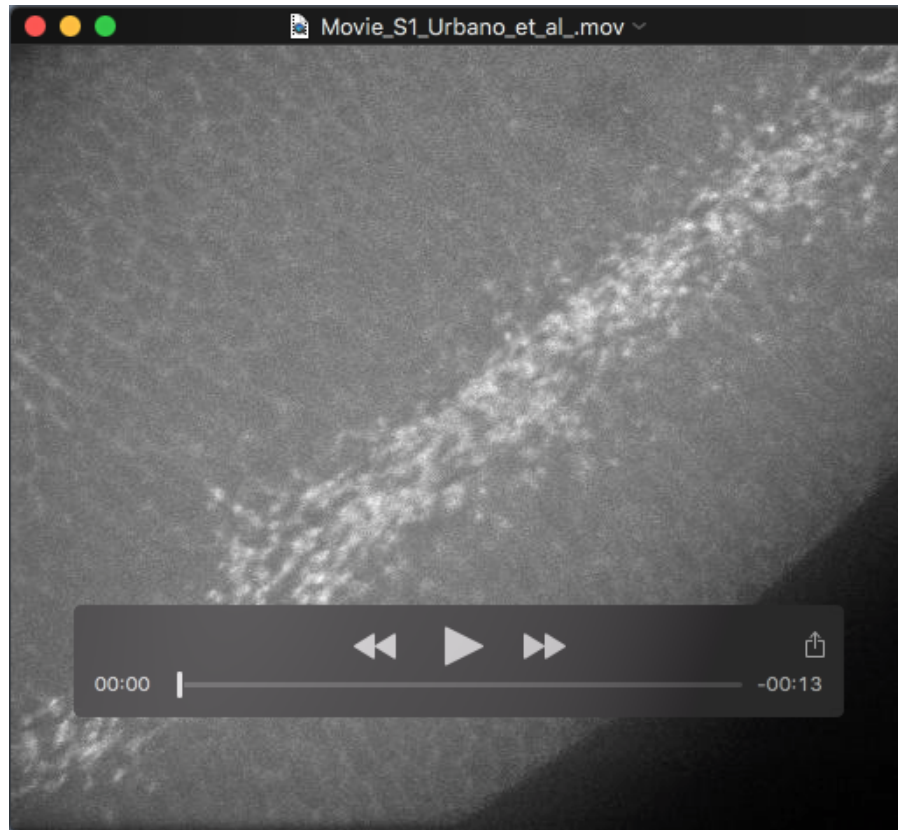


Figure S5: Index of straightness for endogenous and ectopic PSBs above and below adherens junctions. (A,B) Plots of the average index of straightness (IS) measured at different positions along the apicobasal axis (relative to the adherens junctions, AJ) in (A) wildtype and (B) *arm>wg* embryos, for PSB traces (green), control traces one cell away toward the posterior (En side, magenta), control traces one cell toward the anterior (Wg side, blue), and traces along the ectopic PSBs (cyan). $n=3$ embryos of each type. Error bars show $\text{mean} \pm 95\%$ c.i. (C-C'') Confocal images showing the three wildtype embryos used in (A), as a single Z slice from the phalloidin staining, overlaid with the positions of the traces used to measure IS. (D-D'') Plots of average IS vs. apicobasal depth for each embryo in (C-C''), respectively. (E-E'') Confocal images showing the three *arm>wg* embryos used in (B), as a single Z slice from the phalloidin staining, overlaid with the positions of the traces used to measure IS. (F-F'') Plots of the average IS vs. apicobasal depth for each embryo in (E-E''), respectively. Error bars show $\text{mean} \pm 95\%$ c.i. Note that the same 6 embryos are used in Fig.7.



Movie 1: Myosin-II-like localisation of Flw-YFP during mesoderm invagination and early germband extension. Flw-YFP can be seen in the apices of presumptive mesoderm cells, and is present in the medial pulsatile flows at the apical cortex of cells in the extending germband, as well as being planar polarised at their junctions.